

# Music from the heavens - Gravitational waves from supermassive black hole mergers in the EAGLE simulations

Jaime Salcido,<sup>1\*</sup> Richard G. Bower,<sup>1</sup> Tom Theuns,<sup>1</sup> Stuart McAlpine,<sup>1</sup>  
Matthieu Schaller,<sup>1</sup> Robert A. Crain,<sup>2</sup> Joop Schaye,<sup>3</sup> John Regan<sup>1</sup>

<sup>1</sup> *Institute for Computational Cosmology, Department of Physics, Durham University, South Road, Durham, DH1 3LE, UK*

<sup>2</sup> *Astrophysics Research Institute, Liverpool John Moores University, 146 Brownlow Hill, Liverpool L3 5RF, UK*

<sup>3</sup> *Leiden Observatory, Leiden University, P.O. Box 9513, 2300 RA Leiden, the Netherlands*

Accepted XXX. Received YYY; in original form ZZZ

## ABSTRACT

We estimate the expected event rate of gravitational wave signals from mergers of supermassive black holes that could be resolved by a space-based interferometer, such as the Evolved Laser Interferometer Space Antenna (eLISA), utilising cosmological hydrodynamical simulations from the EAGLE suite. These simulations assume a  $\Lambda$ CDM cosmogony with state-of-the-art subgrid models for radiative cooling, star formation, stellar mass loss, and feedback from stars and accreting black holes. They have been shown to reproduce the observed galaxy population with unprecedented fidelity. We combine the merger rates of supermassive black holes in EAGLE with a model to calculate the gravitational waves signals from the intrinsic parameters of the black holes. The EAGLE models predict  $\sim 2$  detections per year by a gravitational wave detector such as eLISA. We find that these signals are largely dominated by mergers between  $10^5 M_{\odot} h^{-1}$  seed mass black holes merging at redshifts between  $z \sim 2.5$  and  $z \sim 0.5$ . In order to investigate the dependence on the assumed black hole seed mass, we introduce an additional model with black hole seed mass an order of magnitude smaller than in our reference model. We find that the merger rate is similar in both models, but that the scenarios could be distinguished through their detected gravitational waveforms. Hence, the characteristic gravitational wave signals detected by eLISA will provide profound insight into the origin of supermassive black holes and the initial mass distribution of black hole seeds.

**Key words:** black hole physics – gravitational waves – cosmology: theory – early Universe – galaxies: formation – galaxies: evolution.

## 1 INTRODUCTION

In our current understanding of extragalactic astrophysics supermassive black holes (SMBHs) reside at the centres of most galaxies at  $z = 0$  and were responsible for powering the luminous quasars observed within the first billion years of the Universe (e.g. Fan 2006; Volonteri & Bellovary 2012). Observations of a tight correlation between the mass of a galaxy’s central SMBH and key properties of its galactic host, such as the bulge mass and stellar velocity dispersion (e.g. Magorrian et al. 1998; Gebhardt et al. 2000; Ferrarese & Merritt 2000; Gültekin et al. 2009), have led to the idea that SMBHs play a major role in the evolution of their host galaxies (e.g. Bower et al. 2006; Volonteri & Bellovary 2011;

Fabian 2012; Alexander & Hickox 2012; Kormendy & Ho 2013). It seems, therefore, that feedback from active galactic nuclei (AGN), galaxy mergers, and the growth of SMBHs are closely intertwined (e.g. Kauffmann & Haehnelt 2000; King 2003; Di Matteo et al. 2005; Booth & Schaye 2009; Fanidakis et al. 2011).

In a standard Lambda Cold Dark Matter ( $\Lambda$ CDM) cosmology cosmic structures build up hierarchically by the continuous merging of smaller structures and the accretion of surrounding matter. In this hierarchical scenario central SMBHs follow a similar build-up process and are the result of a complex evolution, in which black hole (BH) seeds grow both through accretion episodes and mergers with other BHs. However, constraining the formation mechanisms of BHs represents a major observational challenge. The direct detection of gravitational wave (GW) signals from SMBH mergers may be proved to be a viable way to discriminate

\* E-mail: [jaime.salcido@durham.ac.uk](mailto:jaime.salcido@durham.ac.uk)

among the different BH seed formation models (e.g. Volonteri 2010; Amaro-Seoane et al. 2012). The gravitational radiation emitted during the merging of the SMBHs in the centres of colliding galaxies will produce some of the ‘loudest’ events in the Universe, which can provide us with unique information about the nature of BHs and also provides a test of our understanding of gravity and galaxy evolution.

In the last decade major efforts have been made to predict the event rate of GWs in the frequency band of a space-based GW detector such as the Evolved Laser Interferometer Space Antenna (eLISA, Amaro-Seoane et al. 2012, 2013). These predictions range from a few, up to a few hundred events per year, depending on the assumptions underpinning the calculation of the SMBHs coalescence rate. Early works derived the SMBH coalescence rate from observational constraints such as the observed quasar luminosity function (Haehnelt 1994), whilst more recent studies have utilised Monte Carlo realisations and semi-analytical models of the hierarchical assembly of dark matter haloes (e.g. Wyithe & Loeb 2003; Enoki et al. 2004; Koushiappas & Zentner 2006; Sesana et al. 2007). In contrast to semi-analytic models, hydrodynamical simulations follow the dynamics of the cosmic gas by direct numerical integration of the equations of hydrodynamics. Hence a more complete and consistent picture of the evolution of SMBHs and their host galaxies can be obtained, since the emergent predictions for SMBH mergers are not dictated by the assumptions of a semi-analytic model.

The *Evolution and Assembly of GaLaxies and their Environment* (EAGLE) project (Schaye et al. 2015; Crain et al. 2015) consists of a suite of hydrodynamical simulations of a  $\Lambda$ CDM cosmogony. Using state-of-the-art subgrid models for radiative cooling, star formation, stellar mass loss, and feedback from stars and accreting BHs, the simulations reproduce the observed galaxy population with unprecedented fidelity. Key observations, such as the present-day stellar mass function of galaxies, the dependence of galaxy sizes on stellar mass, and the amplitude of the central BH mass-stellar mass relation, as well as many other properties of observed galaxies and the intergalactic medium (both at the present day and at earlier epochs) are reproduced by the simulations (e.g. Bahé et al. 2016; Furlong et al. 2015a,b; Trayford et al. 2015; Schaller et al. 2015a; Lagos et al. 2015; Segers et al. 2015; Rahmati et al. 2015b,a). In this study we introduce the first estimate of the event rate of GWs expected from SMBH mergers utilising hydrodynamical cosmological simulations, the EAGLE simulations. We compute that the event rate of GW signals is low enough to produce a set of events that are resolvable by a space-based interferometer, such as eLISA.

The layout of this paper is as follows: In Section 2 we provide a brief summary of the basic equations of the GW signals produced by the SMBH coalescence process. Section 3 presents a brief overview of the EAGLE simulation suite, including the list of simulations used in this study, a discussion of the BH seeding mechanism and growth, as well as the calculated SMBH merger rates from the simulations. In Section 4 we present the predicted GW signals from the simulations and discuss our main results. We discuss the limitations of our analysis, making some remarks on the simulations and the SMBH seeding model adopted in EAGLE and conclude in Section 5.

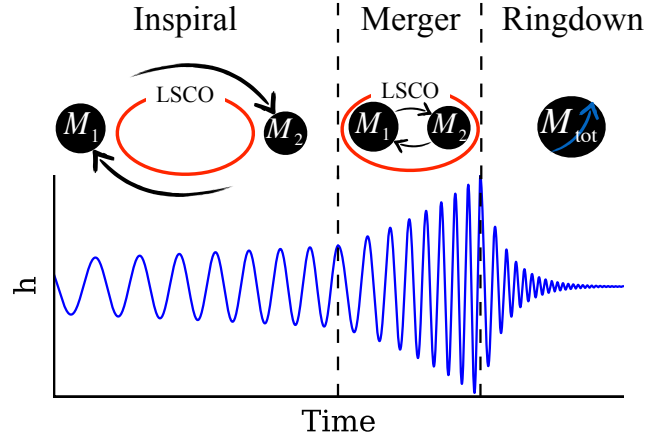


**Figure 1.** Schematic diagram of the phase evolution (inspiral, merger, and ringdown) of a non-spinning SMBH binary coalescence process. The Last Stable Circular Orbit (LSCO) of the binary is shown as the red curve. The resulting SMBH may be rapidly rotating even if the progenitor BHs had very small or no spin (Flanagan & Hughes 1998). Below each phase an example of the *strain* amplitude,  $h$ , as a function of time is shown for the dominant spherical harmonic mode of the GW signal from the non spinning SMBH binary. This specifies the fractional change in the relative displacement between freely falling test masses in a detector due to the GW.

## 2 GRAVITATIONAL WAVE EMISSION FROM SMBH MERGERS

We begin by providing a brief summary of the basic equations of the GW signals produced by the SMBH coalescence process. We refer the reader to Flanagan & Hughes (1998) for a full description of the equations that are presented here. For a general discussion of GW science we refer the reader to Misner et al. (1973) and Schutz & Ricci (2010, Part VIII).

When galaxies merge central SMBHs are brought near the centre of the main halo due to dynamical friction against the dark matter, background stars, and gas. The efficiency of dynamical friction decreases when the SMBHs become close and form a bound binary. In gas rich haloes the orbital evolution is then dominated by the dynamical friction with the surrounding medium, which can effectively dissipate energy and angular momentum from the binary, leading to a short coalescence time-scale ( $\sim 10^7$  yrs). In gas poor systems, the evolution of the binary is largely determined by three-body interactions with the background stars, leading to a long coalescence time-scale ( $\sim 10^8$  yrs). At milliparsec separations GW emission drives the final coalescence process (Sesana 2012).

The BH binary merging process can be divided in three distinct phases which are illustrated by Fig. 1:

(i) The **inspiral phase**, during which the distance between the bound SMBH binary is larger than the Last Stable Circular Orbit ( $R_{\text{LSCO}}$ ) and the mutual gravitational field strength is weak. Since the location of the LSCO is very difficult to calculate for a binary BH system, here  $R_{\text{LSCO}}$  is approximated by the limiting case of a test particle orbiting a non-rotating BH,  $R_{\text{LSCO}} = 6GM_1/c^2 = 3R_s$ , where  $R_s$  is the Schwarzschild radius of the most massive BH in the binary. Post-Newtonian equations provide an accurate representation of the dynamical evolution of the binary in

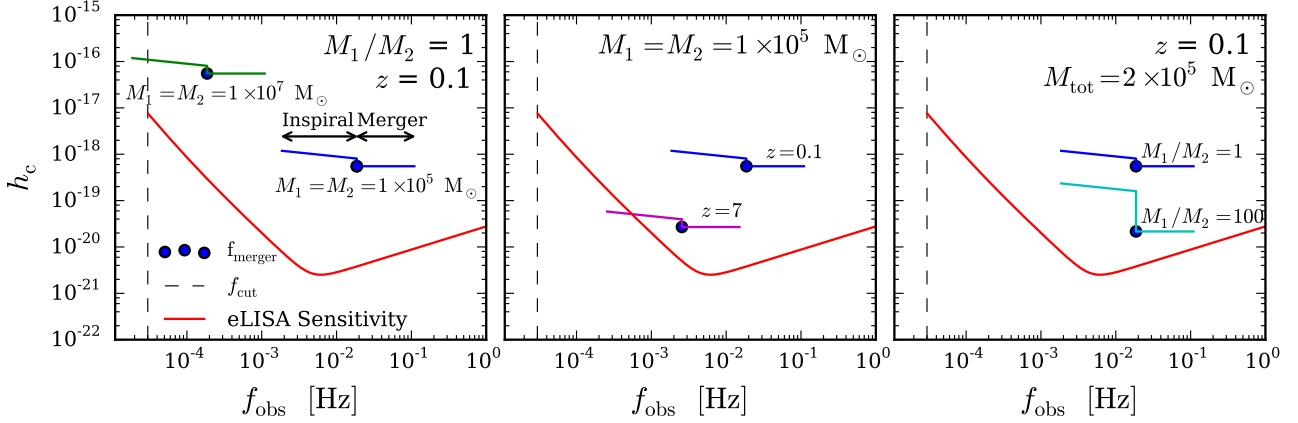


**Figure 2.** Example of the dimensionless characteristic strain amplitude,  $h_c$ , produced by SMBH coalescence events ( $\epsilon_{\text{merger}} = 0.03$ ). In all panels the inspiral and merger phases are shown for an equal mass BH binary (Mass ratio  $M_1/M_2 = 1$ ,  $M_1 = M_2 = 1 \times 10^5 M_\odot$ ) that merge at redshift  $z = 0.1$  as reference (blue line). The frequency at the transition from the inspiral phase to the merger phase ( $f_{\text{merger}}$ ) is highlighted with a blue dot. The sensitivity curve of eLISA was calculated from the analytic approximation provided by [Amaro-Seoane et al. \(2013\)](#). The black dashed line indicates the low-frequency cut-off of the sensitivity curve  $f_{\text{cut}} = 3 \times 10^{-5}$  Hz. GW signals above the sensitivity curve and to the right of the low-frequency cut-off can be resolved from the eLISA data stream. **LEFT PANEL:** The effect of increasing the total mass of the SMBH binary. An equal mass SMBH binary (Mass ratio  $M_1/M_2 = 1$ ) with  $M_1 = M_2 = 1 \times 10^7 M_\odot$  that merges at redshift  $z = 0.1$  is shown in green. **MIDDLE PANEL:** The effect of redshift. An equal mass SMBH binary (Mass ratio  $M_1/M_2 = 1$ ,  $M_1 = M_2 = 1 \times 10^5 M_\odot$ ) merging at redshift  $z = 7$  is shown in magenta. **RIGHT PANEL:** The effect of mass ratio. A BH binary with total mass  $M_{\text{total}} = 2 \times 10^5 M_\odot$  and mass ratio  $M_1/M_2 = 100$  merging at redshift  $z = 0.1$  is shown in cyan.

this phase. The GW signals emitted during the inspiral phase have a characteristic shape with slowly increasing frequency and amplitude.

(ii) In the highly non-linear **merger phase** the SMBHs approach to within the last stable circular orbit ( $\leq R_{\text{LSCO}}$ ) and the dynamics evolve to a rapid plunge and coalescence. In this regime the event horizons of the BHs overlap and the geometry of the local spacetime becomes extremely complicated. Analytical schemes break down in this regime and numerical relativity is needed to model the dynamics through the merger phase.

(iii) Finally, the **quasi-normal-ringdown phase**, where the resulting BH settles down to a rotating Kerr BH emitting GWs due to its deviations from the final axisymmetric state. Perturbation theory can be applied to obtain the quasi-normal modes in this phase. The GW signal emitted during the ringdown phase has a characteristic shape consisting of the superposition of exponentially damped sinusoids.

In this study for simplicity we focus on the inspiral and merger phases of non-spinning SMBH binaries as potential sources of GWs. In general relativity the ‘no-hair’ theorem posits that BHs are completely characterised by only three parameters, namely their mass, spin, and electric charge. For astrophysical BHs the electric charge is usually expected to be negligible ([Misner et al. 1973](#), pp. 875–876). Therefore each coalescing SMBH in our calculations is characterised by three intrinsic parameters, the merger redshift  $z$ , the total mass  $M_{\text{total}} = M_1 + M_2$ , and the mass ratio  $M_1/M_2$  of the binary.  $M_1$  is defined as the more massive member of the BH binary ( $M_1 \geq M_2$ ). In Appendix A we extend our analysis to investigate the case of rapidly spinning coalescing SMBHs.

The inclusion of the signal from the ringdown phase will increase the signal-to-noise ratio (S/N) of observed binaries and enable measurements of the parameters of the resulting SMBH.

## 2.1 Characteristic strain

It is difficult to determine accurately the total gravitational energy radiated as GWs in a BH binary coalescence and modelling the GW signal from these processes still represents a challenge for GW astronomy ([Ohme 2012](#); [Hannam 2014](#)).

In general, the total energy radiated during a BH coalescence will be some fraction,  $\epsilon$ , of the total rest mass energy of the binary ( $M_{\text{total}}c^2$ ) that depends on the mass ratio  $M_1/M_2$ , the orbital angular momentum and the initial spin of the BHs.

The total energy radiated,  $\epsilon$ , can be arbitrarily divided into the energy radiated in each of the BH binary coalescence phases,

$$\epsilon = \epsilon_{\text{inspiral}} + \epsilon_{\text{merger}} + \epsilon_{\text{qnr}}. \quad (1)$$

In GW astronomy it is common to describe the amplitude of a source using the dimensionless *strain* as a function of time,  $h(t)$ . This specifies the fractional change in the relative displacement between two test masses,  $h(t) = \Delta L(t)/L_0$ , where  $L$  is the distance between free-falling masses that constitute the GW detector. The dimensionless characteristic strain amplitude,  $h_c$ , is not the instantaneous strain of a source but rather an accumulated signal, intended to include the effect of integrating a signal during the inspiralling phase. The characteristic strain amplitude,  $h_c$ , is defined as

$$[h_c(f)]^2 = 4f^2 |\tilde{h}(f)|^2, \quad (2)$$

where  $\tilde{h}(f)$  is the Fourier transform of the strain signal,

$\tilde{h}(f) = \mathcal{F}\{h(t)\}(f) = \int_{-\infty}^{\infty} h(t)e^{-2\pi ift} dt$ , and  $f$  is the frequency of the signal (Moore et al. 2015).

In general, the signal-to-noise ratio (S/N) expected to be measured from merging SMBHs by a space-based interferometer depends on the waveform of the GWs, the orientation of the sources with respect to the interferometer, and the direction to the source. If we perform a root mean square (*rms*) average of the amplitude of the GW signals over all possible orientations of the source and interferometer, the S/N will depend only on the total energy spectrum  $dE/df$  radiated by the source (Flanagan & Hughes 1998). The characteristic strain (averaged over source orientations and positions) as a function of the rest-frame frequency  $f_s = f_{\text{obs}}(1+z)$  is then given by

$$h_c(f_{\text{obs}}) = \sqrt{\frac{2G}{c^3}} \frac{(1+z)}{\pi d_L(z)} \sqrt{\frac{dE}{df_s}} \quad (3)$$

$$= 3.24 \times 10^{-27} \frac{(1+z)}{d_L(z)/\text{Mpc}} \sqrt{\frac{dE/df_s}{\text{M}_{\odot} \text{m}^2 \text{s}^{-1}}},$$

where  $d_L(z)$  is the luminosity distance to the BH binary. Note that since the observable of the GW signal is the characteristic strain amplitude,  $h_c$ , as opposed to the energy flux (as is the case for the flux of electromagnetic radiation), it drops off with distance rather than distance squared. In Eq. (3)  $dE/df_s$  is the energy spectrum of GWs emitted by the source. We now discuss the energy spectra of GWs emitted during the inspiral and merger phase of the BH coalescence process.

During the inspiral phase GWs chirp monotonically and the evolution of the binary can be approximated by an adiabatic evolution of circular orbits. The standard quadrupole formula prediction for the inspiral energy spectrum from  $f_{\text{min}}$  to  $f_{\text{merger}}$  is given by

$$\left(\frac{dE}{df_s}\right)_{\text{inspiral}} = \frac{1}{3} \left(\frac{\pi^2 G^2}{f_s}\right)^{1/3} \frac{M_1 M_2}{(M_1 + M_2)^{1/3}} \quad (4)$$

$$= 4.0 \times 10^{21} \left(\frac{\text{Hz}}{f_s}\right)^{1/3} \times \frac{\left(\frac{M_1}{1 \times 10^5 \text{M}_{\odot}}\right) \left(\frac{M_2}{1 \times 10^5 \text{M}_{\odot}}\right)}{\left(\left(\frac{M_1}{1 \times 10^5 \text{M}_{\odot}}\right) + \left(\frac{M_2}{1 \times 10^5 \text{M}_{\odot}}\right)\right)^{1/3}} [\text{M}_{\odot} \text{m}^2 \text{s}^{-1}].$$

The energy spectrum for the merger phase is highly uncertain (Flanagan & Hughes 1998). For simplicity, a flat energy spectrum is often assumed ( $f_s \in (f_{\text{merger}} \leq f_s \leq f_{\text{qnr}})$ ), with amplitude such that the total energy radiated in the merger is a fraction  $\epsilon_{\text{merger}}$  of the total rest mass

$$\left(\frac{dE}{df_s}\right)_{\text{merger}} = \frac{c^2 M_{\text{total}} \xi(M_1, M_2) \epsilon_{\text{merger}}}{f_{\text{qnr}} - f_{\text{merger}}} \quad (5)$$

$$= 9.0 \times 10^{21} \frac{\left(\frac{M_{\text{total}}}{1 \times 10^5 \text{M}_{\odot}}\right) \xi(M_1, M_2) \epsilon_{\text{merger}}}{(f_{\text{qnr}}/\text{Hz}) - (f_{\text{merger}}/\text{Hz})} [\text{M}_{\odot} \text{m}^2 \text{s}^{-1}],$$

where the dimensionless reduction function,  $\xi$ , provides a scaling law that ensures the correct fitting of the energy emitted for all BH mass ratios (Flanagan & Hughes 1998), and is equal to one for equal mass BHs. It is given by

$$\xi(M_1, M_2) = \left(\frac{4\mu}{M_1 + M_2}\right)^2, \quad (6)$$

where the reduced mass  $\mu$  is given by,

$$\mu = M_1 M_2 / (M_1 + M_2). \quad (7)$$

Since the merger phase starts approximately at the last stable circular orbit, we can set the value of the frequency at the transition from the inspiral phase to the merger phase to  $f_{\text{merger}} = f_{\text{LSCO}}$ . However, the location of the LSCO is very difficult to calculate for a binary BH system and the value of  $f_{\text{LSCO}}$  may vary depending on the mass ratio and spin of the BHs merging. Using higher-order post-Newtonian methods Kidder et al. (1993) approximate  $f_{\text{merger}}$  in the absence of a gravitational radiation reaction in the equations of motion and obtain

$$f_{\text{merger}} = (0.02c^3)/(GM_{\text{total}}) \quad (8)$$

$$\simeq \frac{4.1 \times 10^{-2}}{(M_{\text{total}}/1 \times 10^5 \text{M}_{\odot})} [\text{Hz}],$$

which is approximately the frequency at the LSCO of a test particle orbiting a non-rotating BH ( $R_{\text{LSCO}} = 6GM_1/c^2$ ).

The efficiency with which energy is radiated during the merger phase,  $\epsilon_{\text{merger}}$ , depends on the mass of the BHs, their spin, and their orbital angular momentum. Following Flanagan & Hughes (1998), radiative efficiencies of 3% and 10% are reasonable for merging BHs with no spin and rapidly spinning coalescing BHs respectively. For our analysis we have chosen a conservative value of  $\epsilon_{\text{merger}} = 0.03$  for merging BHs with no spin. In Appendix A we discuss the effect seen if the more optimistic value of  $\epsilon_{\text{merger}} = 0.1$  is used.

The loss of energy through GWs leads to a decrease in the separation of the BH binary and hence the orbital frequency increases. For Keplerian circular orbits the frequency of the GWs is twice the orbital frequency ( $f_s = 2f_{\text{orbit}}$ ). Integrating the frequency evolution of the inspiral phase, or chirp,  $\dot{f} = df/dt$ , we can estimate the time it takes for the binary to evolve between any two frequencies. It can be shown (Shapiro & Teukolsky 1983; Tinto 1988) that for BH binaries on Keplerian circular orbits

$$t(f_2) - t(f_1) = \frac{5}{256} \frac{c^5}{G^{5/3}} \frac{(M_1 + M_2)^{1/3}}{M_1 M_2} \times (2\pi)^{-8/3} (f_1^{-8/3} - f_2^{-8/3}). \quad (9)$$

The intrinsic duration of the inspiral phase is then given by

$$\tau_{\text{inspiral}} = t(f_{\text{merger}}) - t(f_{\text{min}}), \quad (10)$$

where the value of  $f_{\text{min}}$  at which the inspiral spectrum starts is uncertain. Since  $f_{\text{merger}}$  is set by Eq. (8)  $f_{\text{min}}$  is a free parameter in our calculations. Clearly, choosing  $f_{\text{min}}$  very close to  $f_{\text{merger}}$  gives short inspiral times. On the other hand,  $f_{\text{min}} \ll f_{\text{merger}}$  will produce the opposite effect. Following the approach of Koushiappas & Zentner (2006), we choose  $f_{\text{min}}$  to be close to  $f_{\text{merger}}$  to ensure reasonable values for the time that the BH binary systems spend in the inspiral phase, which are also comparable to the orbital frequency at the BH binary hardening radius (Quinlan 1996). We have chosen  $f_{\text{min}} = 0.1f_{\text{merger}}$  for our analysis. Substituting  $f_{\text{min}}$  and  $f_{\text{merger}}$  from Eq. (8) in Eq. (10) yields

$$\tau_{\text{inspiral}} \simeq 3.44 \times 10^{-5} \frac{\left[\left(\frac{M_1}{1 \times 10^5 \text{M}_{\odot}}\right) + \left(\frac{M_2}{1 \times 10^5 \text{M}_{\odot}}\right)\right]^3}{\left(\frac{M_1}{1 \times 10^5 \text{M}_{\odot}}\right) \left(\frac{M_2}{1 \times 10^5 \text{M}_{\odot}}\right)} [\text{yrs}], \quad (11)$$



The intrinsic duration of the merger phase is approximated by (Koushiappas & Zentner 2006),

$$\tau_{\text{merger}} \sim 14.7 \left( \frac{M_{\text{total}}}{1 \times 10^5 M_{\odot}} \right) [\text{sec}]. \quad (12)$$

Finally, the resulting SMBH should undergo damped oscillations emitting gravitational radiation due to its asymmetries. The quasi-normal-ringdown frequency will then depend on the final BH mass  $M_{\text{total}}$  and the dimensionless rotation parameter  $a = (c/G)(J/M_{\text{total}}^2)$ , where  $J$  is the resulting BH angular momentum and  $0 \leq a \leq 1$ . Echeverria (1989) developed the analytic fit

$$f_{\text{qnr}} \approx c^3 [1 - 0.63(1 - a)^{(3/10)}] / (2\pi G M_{\text{total}}) [\text{Hz}]. \quad (13)$$

We assume  $a = 0.95$  as the resulting SMBH may be rapidly rotating even if the progenitor BHs had very small or no spin. (Flanagan & Hughes 1998). Then Eq. (13) yields

$$f_{\text{qnr}} \sim \frac{2.41 \times 10^{-1}}{(M_{\text{total}}/1 \times 10^5 M_{\odot})} [\text{Hz}]. \quad (14)$$

In Fig. 2 we show some examples of the dimensionless characteristic strain amplitude  $h_c$  produced by massive BH coalescence events with different masses and occurring at different redshifts, calculated with the equations given in this section.

## 2.2 The eLISA sensitivity curve

The Evolved Laser Interferometer Space Antenna is a space-based mission designed to measure gravitational radiation over a broad band of frequencies ranging between  $f \sim 0.1$  mHz to  $f \sim 1$  Hz. We refer the reader to Amaro-Seoane et al. (2013) for a detailed description of the eLISA concept and architecture. According to the design requirements, the sensitivity that eLISA will be able to achieve in dimensionless characteristic strain noise amplitude is

$$h_n(f_{\text{obs}}) = \sqrt{S_n(f_{\text{obs}}) f_{\text{obs}}}, \quad (15)$$

where the strain noise power spectral density  $S_n(f_{\text{obs}})$  is given by the analytical approximation,

$$S_n(f_{\text{obs}}) = \frac{20}{3} \frac{4 \times S_{\text{acc}}(f_{\text{obs}}) + S_{\text{sn}}(f_{\text{obs}}) + S_{\text{omn}}(f_{\text{obs}})}{L^2} \times \left( 1 + \left( \frac{f_{\text{obs}}}{0.41 \left( \frac{c}{2L} \right)} \right)^2 \right), \quad (16)$$

where  $f_{\text{obs}}$  is the observed frequency and  $L = 1 \times 10^9$  m is the optical path-length between the free-falling masses. At low frequencies the noise spectrum of the instrument is dominated by residual acceleration noise of the test masses caused by force gradients arising due to the relative movement of the spacecraft with respect to the test masses

$$S_{\text{acc}}(f_{\text{obs}}) = 1.37 \times 10^{-32} \left( 1 + \frac{10^{-4} \text{Hz}}{f_{\text{obs}}} \right) \left( \frac{\text{Hz}}{f_{\text{obs}}} \right)^4 [\text{m}^2 \text{Hz}^{-1}]. \quad (17)$$

For  $f_{\text{obs}} \geq 5 \times 10^{-3}$  Hz, the arm length measurement noise dominates, for which the quantum mechanical photon shot noise is

$$S_{\text{sn}}(f_{\text{obs}}) = 5.25 \times 10^{-23} [\text{m}^2 \text{Hz}^{-1}]. \quad (18)$$

At higher frequencies the sensitivity decreases again, due to the arm-length response to multiple wavelengths of GWs.

This effect is included with other combined measurement noise in,

$$S_{\text{omn}}(f_{\text{obs}}) = 6.28 \times 10^{-23} [\text{m}^2 \text{Hz}^{-1}]. \quad (19)$$

The eLISA sensitivity curve obtained from Eq. (15) is plotted as the red curves in Fig. 2.

The measurement frequency bandwidth requirement for the detector is ( $10^{-4}$  Hz to 1 Hz) with a target of ( $3 \times 10^{-5}$  Hz to 1 Hz) (Amaro-Seoane et al. 2013). For our analysis we adopt the target frequency cut  $f_{\text{cut}} = 3 \times 10^{-5}$  Hz. We discuss in Appendix A the impact of changing the low-frequency cut-off of the sensitivity curve calculation, which determines the detectability of the most massive SMBH coalescences. The detector's low-frequency cut is indicated by the vertical black dashed lines in Fig. 2.

## 2.3 Resolved events

An advantage of using the characteristic strain to describe the amplitude of GW sources given the sensitivity of the detector is that the S/N can be written as

$$S/N = \sqrt{\int_f^{f+\Delta f} \left[ \frac{h_c(f'_{\text{obs}})}{h_n(f'_{\text{obs}})} \right]^2 \frac{df'_{\text{obs}}}{f'_{\text{obs}}}}, \quad (20)$$

which allows one to assess by eye the detectability of a given source if  $h_c$  is plotted against the observed frequency (Moore et al. 2015).

The resolution frequency bin,  $\Delta f$ , is set by the minimum frequency resolvable by the instrumentation. It is the inverse of the mission lifetime  $\Delta f \sim 1/T_{\text{obs}}$ , where  $T_{\text{obs}}$  is the length of observation (Gair et al. 2013). For small  $\Delta f$ , we can assume a constant ratio  $k = h_c(f'_{\text{obs}})/h_n(f'_{\text{obs}})$ . Then, by changing the integration limits as  $f + \Delta f = f(1 + \alpha)$ , where  $\alpha = \Delta f/f$ , we can rewrite Eq. (20) as

$$\begin{aligned} (S/N)^2 &= k^2 \int_f^{f(1+\alpha)} \frac{df'_{\text{obs}}}{f'_{\text{obs}}} \\ &= k^2 \ln(1 + \alpha). \end{aligned} \quad (21)$$

The eLISA mission has an expected duration of 3 years. Therefore  $\Delta f \sim 1/T_{\text{obs}} = 1/(3\text{yrs}) \approx 10^{-8}$  Hz. If we impose  $S/N \gtrsim 5$  for all the frequency bandwidth ( $3 \times 10^{-5}$  Hz to 1 Hz) in Eq. (21), this results in  $k \gtrsim 1.76$ . In the examples shown in Fig. 2 it can be seen that once any given GW signal crosses the detector sensitivity curve, the ratio of the signal to the sensitivity curve,  $k$ , rapidly increases by a few orders of magnitude. Therefore we can safely assume that all GW signals above the sensitivity curve (i.e.  $h_c(f_{\text{obs}}) \geq h_n(f_{\text{obs}})$ ) can be detected by eLISA.

## 2.4 Event rate

We calculate the number of detected sources (i.e.  $h_c(f_{\text{obs}}) \geq h_n(f_{\text{obs}})$ ) per redshift interval  $z + \Delta z$  and co-moving volume  $V_c$ , and denote this quantity as  $d^2\bar{n}(z, k \geq 1)/dzdV_c$ . Integrating over all redshifts, the estimated event rate of detected GW sources per observed time is given by

$$\frac{d\bar{N}}{dt_{\text{obs}}} = \int_0^\infty \frac{d^2\bar{n}(z, k \geq 1)}{dzdV_c} \frac{dz}{dt} \frac{dV_c}{dz} \frac{dz}{(1+z)}. \quad (22)$$

The total number of observed events in a given observation time is simply

$$N_{\text{total}} = \int_0^{T_{\text{obs}}} \frac{d\bar{N}}{dt_{\text{obs}}} dt_{\text{obs}}, \quad (23)$$

where  $T_{\text{obs}} = 3$  yrs is the length of the mission. We now seek to estimate this quantity using the merger rates of SMBHs in the EAGLE cosmological hydrodynamical simulations.

### 3 THE EAGLE SIMULATIONS

The EAGLE simulation suite<sup>1</sup> (Schaye et al. 2015; Crain et al. 2015) consists of a large number of cosmological hydrodynamical simulations that include different resolutions, simulated volumes and physical models. These simulations use advanced smoothed particle hydrodynamics (SPH) and state-of-the-art subgrid models to capture the unresolved physics. Radiative cooling (Wiersma et al. 2009a), star formation (Schaye & Dalla Vecchia 2008; Schaye 2004), metal enrichment (Wiersma et al. 2009b), energy input from stellar feedback (Dalla Vecchia & Schaye 2012), BH growth (Rosas-Guevara et al. 2015; Schaye et al. 2015), and feedback from active galactic nuclei (Schaye et al. 2015) are included. The simulation suite was run with a modified version of the GADGET-3 SPH code (last described by Springel 2005) and includes a full treatment of gravity and hydrodynamics. The modifications to the SPH method, collectively referred to as ANARCHY (Dalla Vecchia et al. in prep), make use of the conservative pressure-entropy formulation of SPH derived by Hopkins (2013), the artificial viscosity switch from Cullen & Dehnen (2010), an artificial conduction switch similar to that of Price (2008), the  $C_2$  kernel of Wendland (1995), and the time-step limiters of Durier & Dalla Vecchia (2012). The effects of this state-of-the-art formulation of SPH on the galaxy properties are explored in detail by Schaller et al. (2015b). The calibration strategy is described in detail by Crain et al. (2015) who also presented additional simulations to demonstrate the effect of parameter variations.

The halo and galaxy catalogues for more than  $10^5$  simulated galaxies of the main EAGLE simulations with integrated quantities describing the galaxies, such as stellar mass, star formation rates, metallicities and luminosities, are available in the EAGLE database<sup>2</sup> (McAlpine et al. 2015). A complete description of the code and physical parameters used in the EAGLE simulations can be found in Schaye et al. (2015), here we present a brief overview of the BH seeding and growth mechanisms. Cosmological parameters for a standard  $\Lambda$ CDM universe were adopted by these simulations. The values of the key cosmological parameters implemented are  $\Omega_m = 0.307$ ,  $\Omega_\Lambda = 0.693$ ,  $\Omega_b = 0.04825$ ,  $h = 0.6777$  and  $\sigma_8 = 0.8288$ , as inferred by the Planck Collaboration et al. (2014).

The label for each simulation denotes the comoving cube box length and the cube root of the number of particles in the simulation. For example, Ref-L100N1504 corresponds to a simulation volume of  $(100 \text{ cMpc})^3$  (where cMpc denotes co-moving megaparsecs) using  $1504^3$  particles of dark matter

and an equal number of baryonic particles. A prefix distinguishes the subgrid variations. For example, the prefix ‘Ref-’ refers to a simulation using the reference model.

We compare the predicted GW signals from two EAGLE models, our reference simulation Ref-L100N1504, and a modified version of the Ref-L050N0752 model which uses the same calibrated subgrid parameters as the reference model, but smaller BH seeds, as described in Section 3.1. We have labeled this model SS-L050N0752. Additionally, in order to test for convergence with simulated volume size and resolution, the Ref-L050N0752, Ref-L025N0376 and Recal-L025N0752 models are compared in Appendix A. As discussed by Schaye et al. (2015), the ‘Recal-’ higher-resolution simulation uses values of the subgrid parameters that were recalibrated following the same procedure used for the reference simulation, enabling the user to test the “weak convergence” properties of the simulations. In Table 1 we summarise the simulation models used in this paper, including the comoving cubic box length, initial baryonic and non-baryonic particle masses, gravitational softening lengths and BH seed mass. Together these parameters determine the dynamic range and resolution that can be achieved by the simulations.

#### 3.1 Black hole seeding

To explain the population of luminous quasars in the high-redshift Universe ( $z \geq 6$ ) SMBHs must have formed early and grow rapidly (e.g. Volonteri & Bellovary 2012). Different formation and evolution mechanisms for BH seeds have been proposed to explain the rapid growth that enables these seeds to grow to masses of  $10^9 M_\odot$  in less than one billion years. These SMBHs may have originated from the remnants of the very first generation of stars, runaway collisions of stars and/or stellar mass BHs, direct collapse of supermassive stars, or from an even more exotic process (refer to Volonteri 2010 for a review on formation models for SMBHs). We now briefly review the most promising models for forming SMBH seeds in the early Universe:

##### (i) Remnants of the first generation of stars

BH seeds may have formed from remnants of Population III stars (e.g. Madau & Rees 2001; Volonteri et al. 2003). If stars more massive than  $\sim 250 M_\odot$  formed from primordial gas, they are predicted to directly collapse into BH seeds with masses of  $\sim 100 M_\odot$ . However, it is still unclear if most of the first stars were born with such large masses (e.g. Clark et al. 2011; Greif et al. 2011). Additionally, in order to grow to masses in excess of  $10^9 M_\odot$  as early as redshift  $z \sim 6$  seeds would require to grow close to the Eddington rate for the majority of their lifetime. The shallow potential wells in which Population III stars form makes this scenario rather unattractive (e.g. Johnson et al. 2008; Alvarez et al. 2009; Volonteri et al. 2015).

##### (ii) Collapsing nuclear star clusters

In this model, stellar-dynamical instabilities in protogalactic discs may lead to infall without fragmentation of low metallicity gas, increasing the central galactic density (e.g. Seth et al. 2008; Devecchi & Volonteri 2009; Devecchi et al. 2012; Lupi et al. 2014; Katz et al. 2015). Within the nuclear region a dense stellar cluster forms. As the central cluster undergoes core collapse, runaway collisions of stars

<sup>1</sup> <http://www.eaglesim.org>

<sup>2</sup> <http://www.eaglesim.org/database.php>

Simulation	L	N	$m_{\text{gas}}$	$m_{\text{DM}}$	$\epsilon_{\text{com}}$	$\epsilon_{\text{prop}}$	$m_{\text{seed}}$
	[cMpc]		[ $M_{\odot}$ ]	[ $M_{\odot}$ ]	[ckpc]	[ckpc]	[ $M_{\odot}$ ]
Ref-L100N1504	100	$2 \times 1504^3$	$1.81 \times 10^6$	$9.70 \times 10^6$	2.66	0.70	$1.475 \times 10^5$
SS-L050N0752	<b>50</b>	$2 \times 752^3$	$1.81 \times 10^6$	$9.70 \times 10^6$	2.66	0.70	<b><math>1.475 \times 10^4</math></b>
Ref-L050N0752	<b>50</b>	$2 \times 752^3$	$1.81 \times 10^6$	$9.70 \times 10^6$	2.66	0.70	$1.475 \times 10^5$
Ref-L025N0376	<b>25</b>	$2 \times 376^3$	$1.81 \times 10^6$	$9.70 \times 10^6$	2.66	0.70	$1.475 \times 10^5$
Recal-L025N0752	<b>25</b>	$2 \times 752^3$	<b><math>2.26 \times 10^5</math></b>	<b><math>1.21 \times 10^6</math></b>	<b>1.33</b>	<b>0.35</b>	$1.475 \times 10^5$

**Table 1.** Box-size, number of particles, initial baryonic and dark matter particle mass, co-moving and maximum proper gravitational softening, and BH seed mass for the EAGLE simulations used in this paper. Values in bold differences with the Ref-L100N1504 simulation.

may lead to the formation of a single SMBH seed of mass up to  $\sim 10^3 M_{\odot}$ .

(iii) *Direct collapse of supermassive stars*

It has been proposed that in high-redshift haloes radiation emitted by nearby star-forming galaxies could cause the photo-dissociation of  $\text{H}_2$ . This prevents the temperature of primordial gas from reaching very low values and thus elevates the Jeans mass, allowing the formation of a supermassive star (e.g. Omukai 2001; Sugimura et al. 2014; Regan et al. 2015). Another mechanism to form a supermassive star is by rapid funnelling of low metallicity gas in low angular momentum haloes with global or local dynamical instabilities (e.g. Loeb & Rasio 1994; Koushiappas et al. 2004; Begelman et al. 2008). Once a supermassive star forms its core may collapse to form a small BH within the radiation-pressure-supported object. In this scenario the central BH can accrete the entire envelope and form a SMBH seed of mass  $\sim 10^3 M_{\odot}$  up to  $\sim 10^5 M_{\odot}$ .

Constraining the formation mechanisms of BH seeds represents a major observational challenge. As we will show, the detection of GW signals from SMBH coalescences represents a promising way to discriminate among the different theoretical formation models by determining the mass function of the seed BHs.

Since the SMBH seed formation processes are not resolved by cosmological simulations, it is assumed that every halo above a certain threshold mass hosts a central BH seed. For a comprehensive description of the BH seeding mechanisms in these simulations see Springel et al. 2005, Di Matteo et al. 2008, Booth & Schaye 2009, and Schaye et al. 2015. In the Ref-L100N1504 model high-mass BH seeds<sup>3</sup> ( $m_{\text{seed}} = 1.475 \times 10^5 M_{\odot}$ ) are placed at the centre of every halo with total mass greater than  $m_{\text{halo,th}} = 1.475 \times 10^{10} M_{\odot}$  that does not already contain a BH. For the SS-L050N0752 model the BH seed mass is  $m_{\text{seed}} = 1.475 \times 10^4 M_{\odot}$ . We choose to place BH seeds in haloes of mass  $m_{\text{halo,th}} = 1.475 \times 10^{10} M_{\odot}$  (which corresponds to  $m_{\text{halo,th}} \sim 1.5 \times 10^3 m_{\text{DM}}$  for the reference models and  $m_{\text{halo,th}} \sim 1.2 \times 10^4 m_{\text{DM}}$  for the high-resolution ‘Recal’ model) to ensure that the structure of haloes containing BHs is always well resolved. Halos are selected for seeding by regularly running the Friends-of-Friends (FoF) halo finder on the dark matter distribution, with a linking length equal to 0.2 times the mean inter-particle spacing.

When a halo grows above the threshold mass  $m_{\text{halo,th}}$ , its highest-density gas particle is converted into a collisionless BH particle with subgrid mass  $m_{\text{BH}} = m_{\text{seed}}$ . Since the BH seed mass is usually significantly less than the baryonic particle mass ( $m_{\text{seed}} \ll m_{\text{gas}}$ ), the use of a subgrid mass is nec-

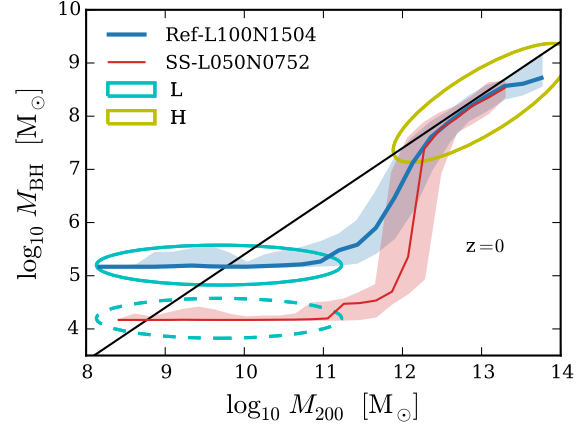


**Figure 3.** Halo mass-central BH mass relation for two EAGLE simulations at redshift  $z = 0$ . Lines represent the median of the distribution for each simulation. Only bins containing 5 objects or more have been plotted. The shaded region encloses the 10<sup>th</sup> to 90<sup>th</sup> percentiles for each model. The black line is shown as reference for a relationship  $M_{\text{BH}} \propto M_{200}$ . Regardless of the initial BH seed mass the halo mass-BH mass relation exhibits a steep slope in haloes with mass  $\sim 10^{12} M_{\odot}$ . At this halo mass the temperature/pressure conditions are optimal for accretion and BHs grow rapidly (Bower et al. in prep). For BHs hosted by haloes more massive than  $\sim 10^{12} M_{\odot}$  the growth is self-regulated by AGN feedback. Two prominent populations of SMBHs are highlighted: BHs not much more massive than the seed mass (**L** for ‘low mass’) and very massive BHs with masses  $> 10^7 M_{\odot}$  (**H** for ‘high mass’).

essary for BH-specific processes such as accretion (Springel et al. 2005). On the other hand, gravitational interactions are computed using the BH particle mass. For BHs with mass  $\leq m_{\text{gas}}$ , the BHs do not dominate the local dynamics and at every time-step, BHs with mass  $< 10$  times the initial gas particle mass  $m_{\text{gas}}$  are re-positioned on the local potential minimum. We limit this process to particles whose velocity relative to the BH is smaller than  $0.25c_s$ , where  $c_s$  is the local sound speed.

### 3.2 Black hole growth

Once seeded, BHs are free to grow via gas accretion at a rate that depends only on the local hydrodynamical properties, namely: the mass of the BH, the local density and temperature of the surrounding gas, the velocity of the BH relative to the ambient gas, and the angular momentum of the gas with respect to the BH. Accretion onto BHs follows a modified version of the Bondi-Hoyle accretion rate which takes into account the circularisation and subsequent viscous

<sup>3</sup>  $m_{\text{seed}} = 1.475 \times 10^5 M_{\odot} = 1 \times 10^5 M_{\odot} h^{-1}$ , where  $h = 0.6777$ .

transport of infalling material, limited by the Eddington rate (as described by Rosas-Guevara et al. 2015).

Additionally, BHs can grow by merging with other BHs. Two BHs merge if they are separated by a distance that is smaller than both the SPH smoothing kernel of the BH,  $h_{\text{BH}}$ , and the gravitational softening length. The BH smoothing length,  $h_{\text{BH}}$ , is chosen such that within a distance  $h_{\text{BH}}$  from the BH there are  $N_{\text{ngb}} = 48$  SPH neighbours (Springel et al. 2005). Furthermore, in order to prevent BHs from merging during fly-by encounters we impose a limit on the allowed relative velocity of BHs to merge, which has to be smaller than the circular velocity at the distance  $h_{\text{BH}}$ ,  $v_{\text{rel}} < \sqrt{GM_1 h_{\text{BH}}^{-1}}$  (where  $G$  is the gravitational constant and  $M_1$  is the mass of the most massive BH in the pair).

It is important to highlight that the sub-grid physics in the EAGLE simulations were calibrated to reproduce the observed galaxy stellar mass function at redshift  $z = 0.1$ , the amplitude of the galaxy stellar mass-central BH mass relation and galaxy sizes (Crain et al. 2015). Although not part of the calibration procedure, Rosas-Guevara et al. (in prep) show that the simulations also reproduce the observed BH mass function at  $z = 0$  and show good agreement with the observed AGN luminosity functions in the hard and soft X-ray bands. Additionally, Trayford et al. (in prep) shows the important role of BH growth in quenching star formation and establishing the high-mass red sequence of galaxies in EAGLE.

Figure 3 shows the halo mass-central BH mass relation at redshift  $z = 0$  for the EAGLE simulations discussed here. The halo mass,  $M_{200}$ , is defined as the total mass within the radius within which the mean density is 200 times the critical density of the Universe.

Regardless of the initial seed mass, BHs that reside in low-mass haloes barely grow. Then, the accretion behaviour changes dramatically in haloes with mass  $\sim 10^{12} M_{\odot}$ . At this halo mass, the temperature/pressure conditions become optimal for accretion, and BHs grow rapidly. The growth of BHs residing in haloes more massive than  $\sim 10^{12} M_{\odot}$  is self-regulated by AGN feedback and BHs reach similar masses regardless of their initial seed mass. The physical origin of this transition is further discussed by Bower et al. (in prep). As a result of this transition there are two prominent populations of SMBHs in the simulations. These are highlighted in the figure: BHs not much more massive than the seed mass (**L** for ‘low mass’) and very massive BHs with masses  $> 10^7 M_{\odot}$  (**H** for ‘high mass’).

### 3.3 Black hole coalescence

For each SMBH merger that takes place in the simulations we store the mass of both SMBHs,  $M_1$  and  $M_2$ , and the redshift  $z$  at which the merger event takes place. On Fig. 4 we show the 2D histogram of the mass of each BH member for all the mergers in the EAGLE simulation models considered here. The total number of BH mergers in each simulation model is indicated in the figure. For Ref-L100N1504 a total of  $N_{\text{BHM}} = 54,850$  BH mergers take place across cosmic time. A factor of  $\approx 8$  fewer mergers occur in the small seeds ( $N_{\text{BHM}} = 7,045$ ) model almost entirely due to the factor of 8 smaller volume of the simulation. Three prominent populations of characteristic SMBH binaries build up. These

are the result of the halo mass-central BH mass relation in EAGLE, shown in Fig. 3. The groups are: SMBH binaries that involve two BHs not much more massive than the seed mass (**L+L**); extreme mass ratio binaries where  $M_1$  is massive ( $> 10^7 M_{\odot}$ ) and  $M_2$  is not much more massive than the seed mass (**L+H**); the case where both BHs are massive, with masses between  $10^7$  and  $10^8 M_{\odot}$  (**H+H**).

In Fig. 5 we show the co-moving number density distribution as a function of the more massive member of the BH binaries,  $M_1$ , plotted for five non-contiguous ranges in the mass of the least massive member,  $M_2$ . The (**L+L**) and (**L+H**) populations of binaries correspond to the left and right peaks of the distribution in the top two panels. The population (**H+H**) is shown in the bottom two panels. Naturally, the larger simulation volume samples more massive structures, hence the observed BH coalescence distribution in each panel extends to higher values of  $M_1$ . Since we keep the same vertical axis range for all five panels we can compare the contribution of each mass bin to the total SMBH merger rate. The population of binaries where both BHs are massive (**H+H**), shown in the bottom panel, is at least two orders of magnitude smaller than that of extreme mass binaries (**L+H**) and SMBH binaries that involve two BHs not much more massive than the seed mass (**L+L**), shown in the top two panels of the figure.

## 4 PREDICTED GRAVITATIONAL WAVE EVENT RATE

In order to compute the expected GW signals from SMBH mergers in the simulations, we adopt the following strategy. We first calculate the frequency at the transition from the inspiral phase to the merger phase,  $f_{\text{merger}}$ , for each merger event in EAGLE using Eq. (8). From  $f_{\text{merger}}$  we compute the minimum inspiral frequency  $f_{\text{min}} = 0.1 f_{\text{merger}}$ . We also calculate the frequency at which the merger phase finishes,  $f_{\text{qnr}}$ , using Eq. (13). Assuming that both SMBHs in the binary have no spin, we use Eqs. (3) to (6) to compute the characteristic strain amplitude of the GWs from each binary, which depends only on the merging redshift  $z$  and the mass of each SMBH,  $M_1$  and  $M_2$ . We compute the sensitivity curve of eLISA using the analytical approximation given in Eqs. (15) to (19). For our analysis we adopt the target frequency cut of the detector,  $f_{\text{cut}} = 3 \times 10^{-5}$  Hz. From all the computed GW signals, we filter the events that would be resolvable by the detector using Eq. (21) with a ratio of the signal to the sensitivity curve  $k \geq 1$  (i.e.  $S/N \geq 5$ ). For all resolvable events we compute the observed duration  $\tau_{\text{obs}} = \tau_{\text{inspiral,obs}} + \tau_{\text{merger,obs}}$  using Eqs. (11) and (12). Finally, from the number of resolvable sources we estimate the event rate of GW sources and the total number of expected observable events during the lifetime of the eLISA mission using Eqs. (22) and (23).

For SMBH binaries the S/N of the GW signals is accumulated in the last month of the inspiral phase (Sesana et al. 2011). Therefore, in this study we choose to only include sources that “merge” during the mission time, i.e., to construct the expected event rate we only consider events with  $\tau_{\text{obs}} \leq T_{\text{obs}}$ . In Fig. 6 we show the distribution of the observed duration for all the resolvable events. The performance of the detector improves as a function of the duration of mission and gaps in the data stream would affect the



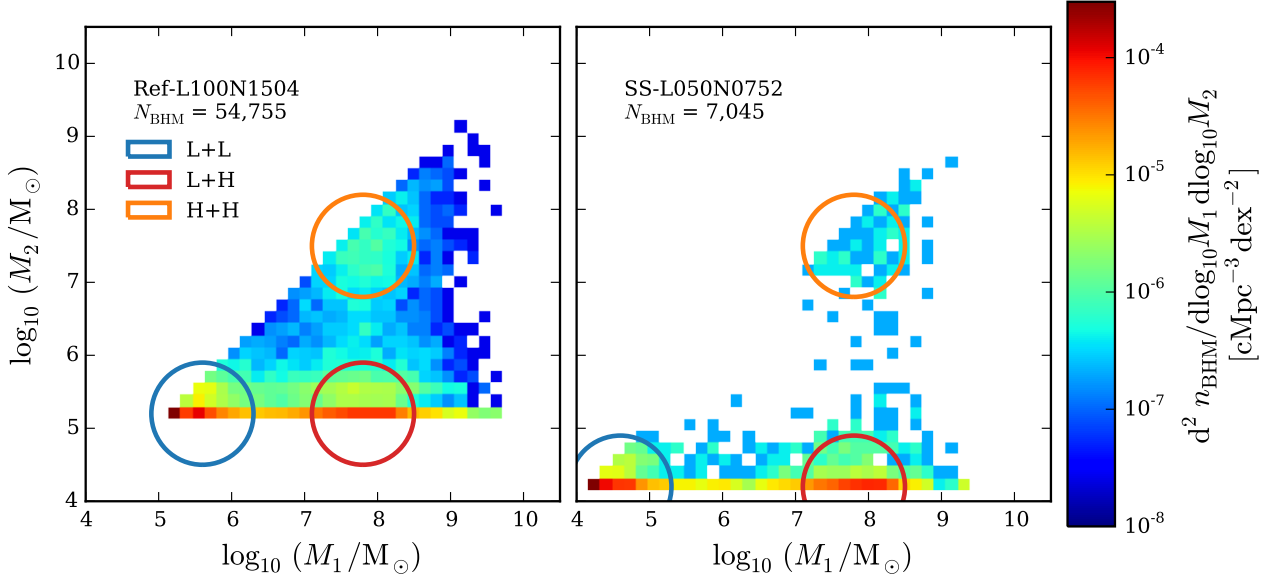


**Figure 4.** 2D histogram of all BH mergers for all redshifts in the EAGLE simulations. Ref-L100N1504 (left panel) and SS-L050N0752 (right panel).  $M_1$  is the more massive member of the SMBH binary ( $M_1 \geq M_2$ ). The total number of coalescence events in each simulation model,  $N_{\text{BHM}}$ , is shown in the top left corner of each panel. Colour coding represents the number density of SMBH mergers per binary mass bin. As a result of the transition in the Halo mass-central BH mass relation shown in Fig. 3, there are three prominent populations of SMBH binaries in the simulations, which are highlighted in the figure: SMBH binaries that involve two BHs not much more massive than the seed mass (**L+L**); extreme mass ratio binaries where  $M_1$  is massive ( $> 10^7 M_\odot$ ) and  $M_2$  is not much more massive than the seed mass (**L+H**); the case where both BHs are massive, with masses above  $10^7 M_\odot$  (**H+H**). Since the populations of high-mass SMBHs in both simulation models reach similar masses (Fig. 3), the population of (**H+H**) binaries occupies the same region in both models. On the other hand, both the (**L+L**) and (**L+H**) populations are shifted in  $M_1$  and  $M_2$  in the SS-L050N0752 model compared to Ref-L100N1504.

number of resolved events (e.g. Sesana et al. 2011). For this study we assume a fiducial eLISA mission continuous lifetime of  $T_{\text{obs}} = 3\text{yrs}$ . We show in Figs. 7 and 8 the characteristic strain amplitude as a function of the observed merger frequency for all the GW events produced by SMBH coalescences in the EAGLE Ref-L100N1504 and SS-L050N0752 simulations respectively. To help visualise the mass range and redshift of BH coalescences that would be detected by eLISA, grey lines indicate the characteristic strain and observed merger frequency emitted by equal mass BH binaries ( $M_1 = M_2$ ) coalescing at different redshifts  $z$ . The following characteristic features can be seen in the figures:

(i) For both models, the most densely populated region of events ( $2 \times 10^{-3} \lesssim f_{\text{mer,obs}}/[\text{Hz}] \lesssim 1.3 \times 10^{-2}$  and  $4 \times 10^{-20} \lesssim h_c \lesssim 1 \times 10^{-18}$  for Ref-L100N1504 and  $2 \times 10^{-2} \lesssim f_{\text{mer,obs}}/[\text{Hz}] \lesssim 1.3 \times 10^{-1}$  and  $4 \times 10^{-21} \lesssim h_c \lesssim 1 \times 10^{-19}$  for SS-L050N0752) corresponds to SMBH binaries where both BHs have masses not much greater than the seed mass (**L+L**). As illustrated in Fig. 2, we expect higher GW frequencies and smaller strain amplitudes from less massive BH mergers. Therefore, for the small seeds model the (**L+L**) population shifts to higher frequencies and lower amplitudes compared to the reference model. For both Ref-L100N1504 and SS-L050N0752 EAGLE models the (**L+L**) population of events occupies a region above the detection threshold of eLISA and hence will provide a high contribution to the data stream (as seen in Fig. 10).

(ii) The second most populated region of events ( $1 \times 10^{-5} \lesssim f_{\text{mer,obs}}/[\text{Hz}] \lesssim 1 \times 10^{-4}$  and

$1 \times 10^{-19} \lesssim h_c \lesssim 1 \times 10^{-18}$  for Ref-L100N1504 and  $1 \times 10^{-5} \lesssim f_{\text{mer,obs}}/[\text{Hz}] \lesssim 1 \times 10^{-4}$  and  $1 \times 10^{-20} \lesssim h_c \lesssim 1 \times 10^{-19}$  for SS-L050N0752) corresponds to binaries from the (**L+H**) population. This population is also shifted to lower amplitudes for the small seeds model relative to the reference model. For both Ref-L100N1504 and SS-L050N0752 EAGLE models most of the events from the (**L+H**) population fall below the detection threshold of eLISA and hence will not contribute significantly to the data stream.

(iii) Few events from the (**H+H**) population occupy a region above the detection threshold of eLISA. However, there are significantly fewer events in this population of binaries compared to the (**L+L**) and (**L+H**) populations (at least two orders of magnitude fewer events, as seen in Fig. 5). Therefore, the binaries from the (**H+H**) population do not show up as a dense region in the plot.

The characteristic shift in amplitude and frequency of the detected GW signals that results from the different SMBH seed masses suggests that eLISA will be a powerful tool to discriminate between different SMBH seeding mechanisms. In Fig. 9 we show the number of detected SMBH coalescences observed per year at redshift  $z = 0$  as a function of the frequency at the transition between the inspiral phase and the merger phase,  $f_{\text{mer,obs}}$ . The figure shows a shift of a decade in frequency of the whole distribution between the simulation models. The amplitude of the peak of the distribution is, however, the same for both models. For lower frequencies (i.e. more massive mergers) the SS-L050N0752 model has fewer detected events ( $\sim 0.3\text{dex}$ ) because these

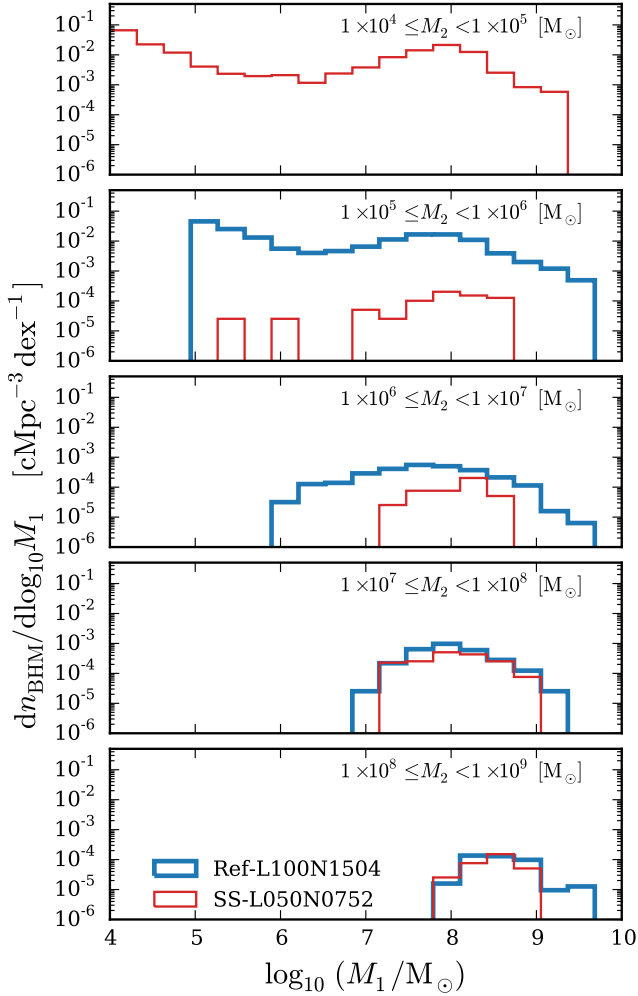


**Figure 5.** Co-moving number density of the more massive member of the BH binaries with mass  $M_1$ , for five non-contiguous ranges in the mass of the least massive member,  $M_2$ , as indicated in the legend (top to bottom). The population of SMBH binaries that involve a BH not much more massive than the seed mass ( $< 10^6 M_\odot$ ) are then shown in the top panel. Binaries where both BHs are massive ( $> 10^7 M_\odot$ ) are shown in the two bottom panels. The population (H+H), shown in the two bottom panels, is at least two orders of magnitude smaller than the (L+L) and (L+H) populations, shown in the top two panels.

events have lower characteristic strain amplitude and therefore some fall below the detection threshold of the eLISA sensitivity curve.

For the signals detected by eLISA it will be possible to extract the physical parameters of the BH sources, such as their masses, luminosity distance, and sky locations, using a set of theoretical templates for the waveforms for each phase (i.e. inspiral, merger, and ringdown phases) (Cutler & Flanagan 1994; Flanagan & Hughes 1998; Amaro-Seoane et al. 2013). In Fig. 10 we have plotted the redshift distribution, the mass function of the more massive member of the binary,  $M_1$ , and the distribution of the mass ratio,  $M_1/M_2$ , of the number of detected SMBH coalescences per observed year at redshift  $z = 0$  (left, central and right panels respectively).

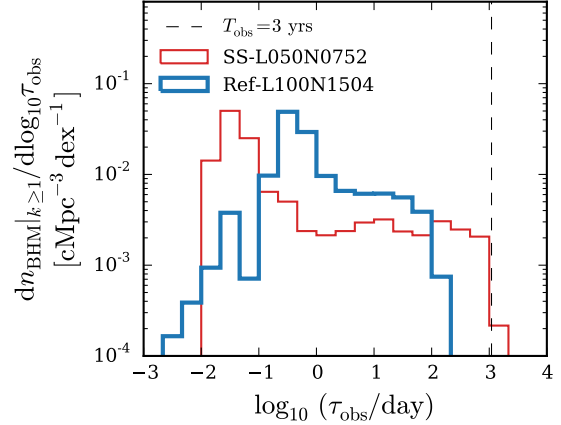


**Figure 6.** Distribution of the observed duration of the events that would be resolvable by the eLISA detector (i.e. the ratio of the GW signal to the detector’s sensitivity curve  $k \geq 1$ ). For our study, we assume an eLISA mission lifetime of  $T_{\text{obs}} = 3$  yrs (dashed vertical line). We only consider events with  $\tau_{\text{obs}} \leq T_{\text{obs}}$  in the rest of the paper.

From the first panel it is clear that SMBHs merging between redshift  $z \sim 2.5$  and  $z \sim 0.5$  will provide the greatest contribution to the event rate of GW signals in both EAGLE models. On the basis of the redshift distributions of detected signals it is thus not possible to discriminate between the SMBH seeding mechanisms implemented in our simulations. The  $M_1$  mass function of the predicted event rate has a very pronounced peak at the SMBH seed mass  $m_{\text{seed}}$  ( $10^5 M_\odot h^{-1}$  for the ‘Ref-’ model and  $10^4 M_\odot h^{-1}$  for the ‘SS-’ model). Given the logarithmic scale of the plot, the galaxy formation model implemented in EAGLE predicts that GW signals will be dominated by the coalescence of BH seeds, which is also shown in the last panel of the figure, in which the mass ratio distribution peaks for equal mass SMBH coalescences for both models. This is a remarkable result, since it implies that the physical parameters of the GW sources recovered from the eLISA data stream will provide us with a profound insight into the nature of SMBHs and the initial mass distribution of seeds.

We use Eq. (22) to calculate the event rate of GW signals resolved by the eLISA mission. We find that for our fiducial model ( $f_{\text{cut}} = 3 \times 10^{-5}$  Hz and  $\epsilon_{\text{merger}} = 0.03$ ) the estimated event rate of GWs is  $\sim 2$  events per year for the inspiral and the merger phases (for both Ref-L100N1504 and SS-L050N0752 simulations). We estimate that in a 3 year mission the eLISA detector should be able to resolve  $\sim 6$  mergers and  $\sim 6$  inspiral signals from SMBH mergers. Even with this low event rate the information carried by each gravitational waveform would provide us with a powerful tool to constrain the SMBH seed formation mechanisms.

## 5 DISCUSSION AND CONCLUSIONS

Using the EAGLE simulations, a state-of-the-art cosmological hydrodynamical simulation suite, we have computed the event rate of GW signals expected from SMBH mergers that should be resolved by a space-based GW detector such as the Evolved Laser Interferometer Space Antenna, eLISA.

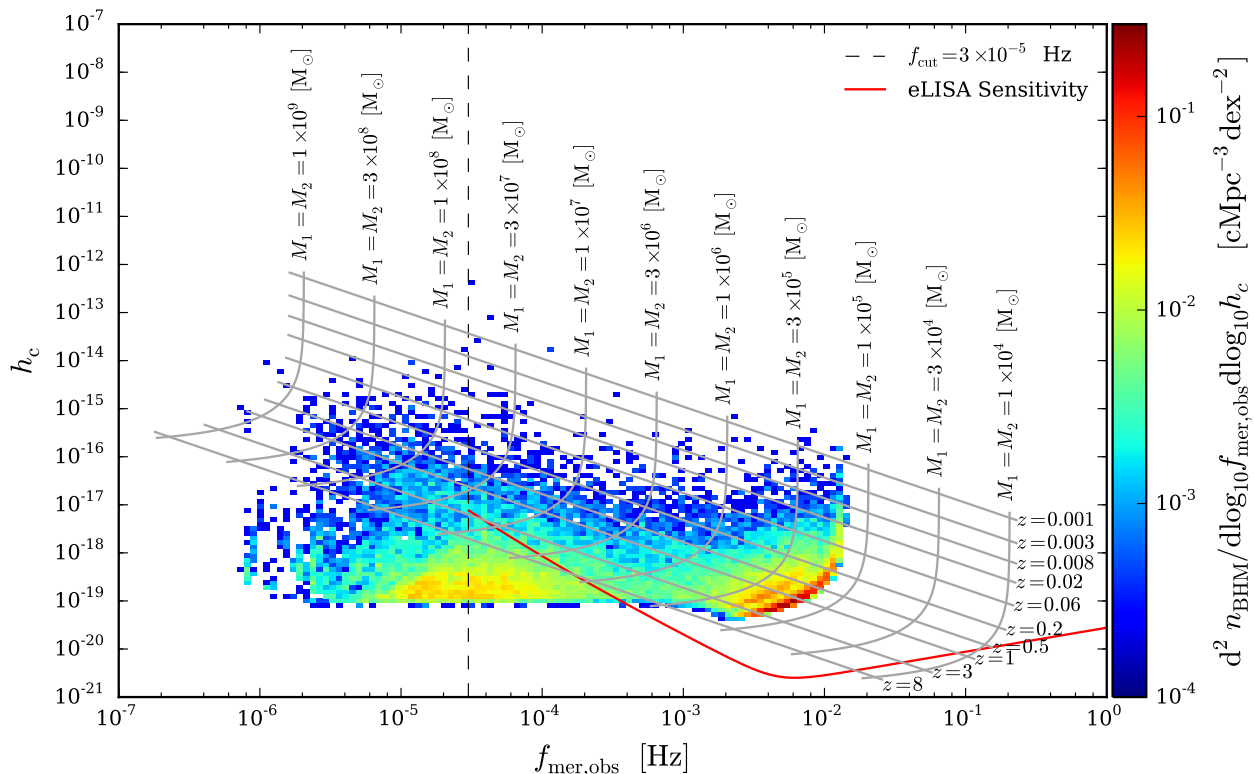


**Figure 7.** Characteristic strain amplitude  $h_c$  of the GW signals emitted by all SMBH coalescences in the EAGLE Ref-L100N1504 simulation as a function of the observed frequency at the transition between the inspiral phase and the merger phase of the SBMH coalescence process  $f_{\text{mer,obs}}$ . Colour coding represents the co-moving number density of events per characteristic strain-observed merger frequency bin. Grey contour lines indicate the characteristic strain and observed merger frequency for equal mass BH binaries ( $M_1 = M_2$ ) coalescing at different redshifts  $z$ . The sensitivity curve of eLISA calculated from the analytic approximation in Eq. (15) is shown in red. The black dashed line indicates the low-frequency cut-off of the sensitivity curve  $f_{\text{cut}} = 3 \times 10^{-5}$  Hz. GW signals above the sensitivity curve and to the right of the low-frequency cut-off can be resolved from the eLISA data stream.

The EAGLE simulations use advanced smoothed particle hydrodynamics and physically motivated subgrid models to capture the unresolved physics. These simulations reproduce the observed galaxy population with unprecedented fidelity, providing a powerful tool to study galaxy formation and evolution.

A number of SMBH seed formation mechanisms have been proposed to explain the observed population of high-redshift quasars in our Universe. These mechanisms predict different initial mass functions of BHs seeds. These characteristic BH seed mass functions and the dynamical evolution that takes place during the merging process of SMBH binaries in the centres of colliding galaxies leave a unique imprint on the GW signals predicted by the models. Therefore, the information carried by the gravitational waveforms detected by a GW detector such as eLISA will provide us with a powerful tool to discriminate between different SMBH seeding models.

Since the processes involved in the SMBH seed formation models are not resolved by the simulations, we assume that seed BHs are produced sufficiently frequently that every halo above a certain threshold mass contains a central BH seed. In order to investigate the dependence on the assumed BH seed mass we used two simulation models using BH seeds that differ by an order of magnitude in mass. For the Ref-L100N1504 model, high-mass BH seeds

( $m_{\text{seed}} = 1.475 \times 10^5 M_\odot$ ) were placed at the centre of every halo with total mass greater than  $m_{\text{halo,th}} = 1.475 \times 10^{10} M_\odot$  that did not already contain a BH. For the SS-L050N0752 model, the BH seed mass used was  $m_{\text{seed}} = 1.475 \times 10^4 M_\odot$ . These BH seeds then grow by accreting gas and by mergers with other BHs. Three prominent populations of characteristic SMBH binaries build up in the simulations as a result of the halo mass-central BH mass relation in EAGLE shown in Fig. 3. The groups are: SMBH binaries that involve two BHs not much more massive than the seed mass (**L+L**); extreme mass ratio binaries in which one BH is massive ( $> 10^7 M_\odot$ ) and the other is not much more massive than the seed mass (**L+H**); the case where both BHs are massive, with masses between  $10^7$  and  $10^8 M_\odot$  (**H+H**).

We calculated that the merger rate of SMBHs is similar in both simulation models and will produce a low event rate of GW signals, nonetheless observable by a space-based interferometer such as eLISA. We find that the predicted event rate of GWs for the inspiral and merger phases for both the ‘Ref.’ and ‘SS-’ models is  $\sim 2$  events per year. Hence, in a 3 year mission the eLISA detector should be able to resolve  $\sim 6$  mergers and  $\sim 6$  inspiral signals from SMBH coalescences. Our analysis shows that these signals will be dominated by the coalescence of BH seeds (**L+L** population of binaries) merging between redshifts  $z \sim 2.5$  and  $z \sim 0.5$ . Given the difference in the BH seed mass of the models,

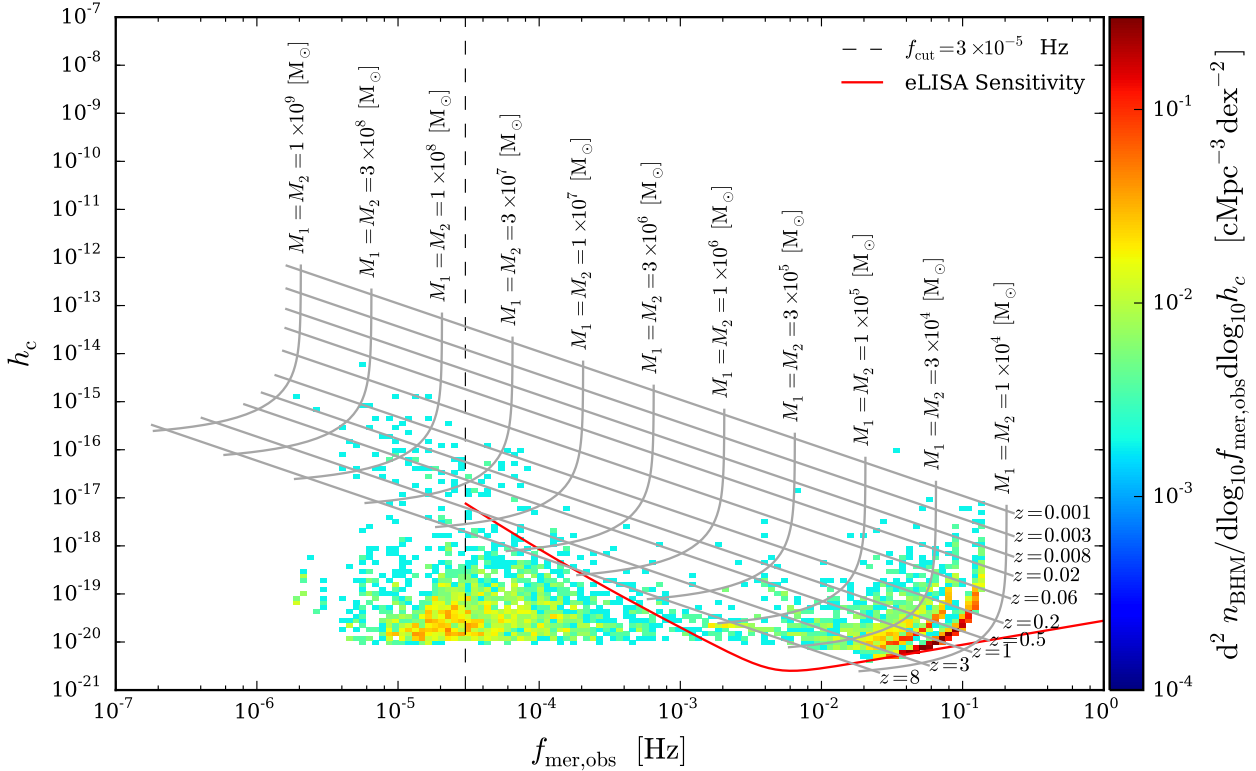


**Figure 8.** As Fig. 7 but for the EAGLE SS-L050N0752 simulation.

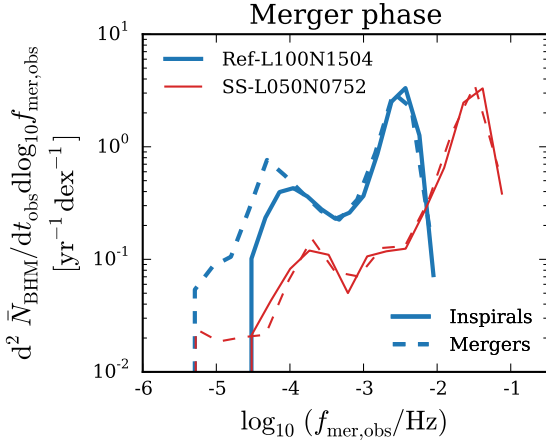


**Figure 9.** Number of detected SMBH coalescences per observed year as a function of the frequency at the transition between the inspiral phase and the merger phase  $f_{\text{mer,obs}}$ . A shift of a decade in frequency of the whole distribution is observed for the SS-L050N0752 compared to the Ref-L100N1504 model. The amplitude of the peak of the distribution is the same for both models. For lower frequencies (i.e. more massive mergers), the SS-L050N0752 model has fewer detected events (by about 0.3 dex) because these events have lower characteristic strain amplitude (as shown in Figs. 7 and 8) and therefore fall outside the detection threshold of the eLISA sensitivity curve.

there is a characteristic shift of a decade in the observed frequency of the whole distribution of the GW signals (Fig. 9). Hence, different physical BH seeding mechanisms could be

distinguished from the detected gravitational waveforms, allowing eLISA to provide us with profound insight into the origin of SMBHs and the initial mass distribution of SMBH seeds (Fig. 10).

We find that EAGLE predicts GW signals that would be best detected by eLISA, but complementary observations of GW signals in different frequency windows will enable us to fully characterise the cosmic history of SMBHs (Crowder & Cornish 2005; Sesana et al. 2008; Janssen et al. 2015; Moore et al. 2015). For instance, pulsar timing arrays will be able to detect GWs in a lower frequency window (i.e.,  $f_{\text{obs}} < 10^{-6}$  [Hz] with  $h_c > 10^{-17}$ , Hellings & Downs 1983; Sesana et al. 2008) than the SMBH mergers arising in our cosmological volume (Fig. 7). On the other hand, if the initial mass function of SMBH seeds extends to masses  $< 10^4 M_{\odot}$ , intermediate frequency missions (i.e.  $10^{-3} \lesssim f_{\text{obs}} / [\text{Hz}] \lesssim 10^1$  with  $h_c > 10^{-25}$ ), like the proposed Advanced Laser Interferometer Antenna (ALIA, Bender et al. 2013), the Big Bang Observer (BBO, Harry et al. 2006), and the Deci-hertz Interferometer GW Observatory (DECIGO, Kawamura et al. 2006), will be suitable to detect the mergers of seeds and shed light on their initial mass function. It is also important to highlight that other GW sources, such as galactic white dwarf binaries, will also contribute to the eLISA data stream.

Since the EAGLE simulations reproduce a wide set of observational properties of the galaxy population we may expect the physics of the real Universe to be reasonably well captured by the phenomenological sub-grid models implemented in the simulations. Nevertheless, the predicted GW event rate is specific to the galaxy formation and evolution model implemented in these simulations and the sub-grid



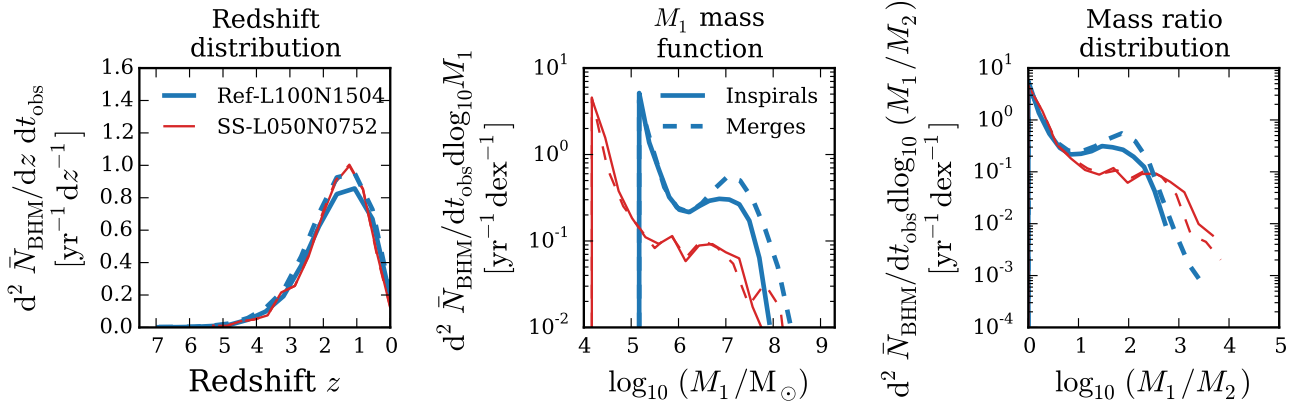


**Figure 10.** *LEFT PANEL:* Redshift distribution of the SMBH coalescences resolved by eLISA. The distribution peaks between redshift  $z \sim 2$  and  $z \sim 1$  for both the inspiral and the merger phases for both EAGLE simulation. *MIDDLE PANEL:* Mass distribution of the more massive member of the binary,  $M_1$ , for the SMBH coalescences resolved by eLISA. For both models, the mass function peaks at  $M_1 \sim m_{\text{seed}}$  for both the inspiral and the merger phases. *RIGHT PANEL:* Distribution of the mass ratio  $M_1/M_2$  of the SMBH coalescences resolved by eLISA. The distribution peaks for equal mass SMBH binaries for both EAGLE simulation models.

models for BH seeding and growth via accretion and mergers. In particular, in the EAGLE simulations BH seeds are placed into haloes of mass  $m_{\text{halo,th}} = 10^{10} M_{\odot}$ , which corresponds to a very small galaxy of stellar mass  $m_* \sim 10^7 M_{\odot}$ . From observational constraints such galaxies are thought to be the smallest galaxies to host SMBHs (Reines et al. 2013; Seth et al. 2014). If BH seeds form efficiently in even lower-mass galaxies, the SMBH mergers would be more common and therefore increase our predicted GW event rate. Our predicted rates are therefore conservative. Addressing this issue in more depth would require a simulation of considerably higher resolution (and yet comparable cosmological volume) coupled to a physical model of BH seed formation. Such a simulation is currently beyond the scope of cosmological simulation codes. Fortunately, since our models predict that eLISA should be very sensitive to the initial mass distribution of BH seeds, it will probe precisely these issues and directly compliment theoretical developments. Further work using the EAGLE simulations, coupled to physical models of BH seed formation could be used to predict the GW signals from SMBH mergers that could be detected by future GW detectors.

## ACKNOWLEDGEMENTS

We are grateful to all members of the Virgo Consortium and the EAGLE collaboration who have contributed to the development of the codes and simulations used here, as well as to the people who helped with the analysis.

This work was supported by the Science and Technology Facilities Council (grant number ST/F001166/1); European Research Council (grant numbers GA 267291 “Cosmiway” and GA 278594 “GasAroundGalaxies”) and by the Interuniversity Attraction Poles Programme initiated by the Belgian Science Policy Office (AP P7/08 CHARM). RAC is a Royal Society University Research Fellow.

This work used the DiRAC Data Centric system at Durham University, operated by the Institute for Computational Cosmology on behalf of the STFC DiRAC

HPC Facility (<http://www.dirac.ac.uk>). This equipment was funded by BIS National E-infrastructure capital grant ST/K00042X/1, STFC capital grant ST/H008519/1, and STFC DiRAC Operations grant ST/K003267/1 and Durham University. DiRAC is part of the National E-Infrastructure. We acknowledge PRACE for awarding us access to the Curie machine based in France at TGCC, CEA, Bruyères-le-Châtel.

Jaime Salcido gratefully acknowledges the financial support from the Mexican Council for Science and Technology (CONACyT), Fellow No. 218259.

## REFERENCES

- Alexander D. M., Hickox R. C., 2012, *New Astron. Rev.*, **56**, 93
- Alvarez M. A., Wise J. H., Abel T., 2009, *ApJ*, **701**, L133
- Amaro-Seoane P., et al., 2012, *Classical and Quantum Gravity*, **29**, 124016
- Amaro-Seoane P., et al., 2013, *GW Notes*, Vol. 6, **6**, 4
- Bahé Y. M., et al., 2016, *MNRAS*, **456**, 1115
- Begelman M. C., Rossi E. M., Armitage P. J., 2008, *MNRAS*, **387**, 1649
- Bender P. L., Begelman M. C., Gair J. R., 2013, *Classical and Quantum Gravity*, **30**, 165017
- Booth C. M., Schaye J., 2009, *MNRAS*, **398**, 53
- Bower R. G., Benson A. J., Malbon R., Helly J. C., Frenk C. S., Baugh C. M., Cole S., Lacey C. G., 2006, *MNRAS*, **370**, 645
- Clark P. C., Glover S. C. O., Smith R. J., Greif T. H., Klessen R. S., Bromm V., 2011, *Science*, **331**, 1040
- Crain R. A., et al., 2015, *MNRAS*, **450**, 1937
- Crowder J., Cornish N. J., 2005, *Phys. Rev. D*, **72**, 083005
- Cullen L., Dehnen W., 2010, *MNRAS*, **408**, 669
- Cutler C., Flanagan É. E., 1994, *Phys. Rev. D*, **49**, 2658
- Dalla Vecchia C., Schaye J., 2012, *MNRAS*, **426**, 140
- Devecchi B., Volonteri M., 2009, *ApJ*, **694**, 302
- Devecchi B., Volonteri M., Rossi E. M., Colpi M., Portegies Zwart S., 2012, *MNRAS*, **421**, 1465
- Di Matteo T., Springel V., Hernquist L., 2005, *Nature*, **433**, 604
- Di Matteo T., Colberg J., Springel V., Hernquist L., Sijacki D., 2008, *ApJ*, **676**, 33
- Durier F., Dalla Vecchia C., 2012, *MNRAS*, **419**, 465

- Echeverria F., 1989, *Phys. Rev. D*, **40**, 3194
- Enoki M., Inoue K. T., Nagashima M., Sugiyama N., 2004, *ApJ*, **615**, 19
- Fabian A. C., 2012, *ARA&A*, **50**, 455
- Fan X., 2006, *New Astron. Rev.*, **50**, 665
- Fanidakis N., Baugh C. M., Benson A. J., Bower R. G., Cole S., Done C., Frenk C. S., 2011, *MNRAS*, **410**, 53
- Ferrarese L., Merritt D., 2000, *ApJ*, **539**, L9
- Flanagan E. E., Hughes S. A., 1998, *Phys. Rev. D*, **57**, 4535
- Furlong M., et al., 2015a, preprint, ([arXiv:1510.05645](#))
- Furlong M., et al., 2015b, *MNRAS*, **450**, 4486
- Gair J. R., Vallisneri M., Larson S. L., Baker J. G., 2013, *Living Reviews in Relativity*, **16**, 7
- Gebhardt K., et al., 2000, *ApJ*, **539**, L13
- Greif T. H., Springel V., White S. D. M., Glover S. C. O., Clark P. C., Smith R. J., Klessen R. S., Bromm V., 2011, *ApJ*, **737**, 75
- Gültekin K., et al., 2009, *ApJ*, **698**, 198
- Haehnelt M. G., 1994, *MNRAS*, **269**, 199
- Hannam M., 2014, *General Relativity and Gravitation*, **46**, 1767
- Harry G. M., Fritschel P., Shaddock D. A., Folkner W., Phinney E. S., 2006, *Classical and Quantum Gravity*, **23**, 4887
- Hellings R. W., Downs G. S., 1983, *ApJ*, **265**, L39
- Hopkins P. F., 2013, *MNRAS*, **428**, 2840
- Janssen G., et al., 2015, *Advancing Astrophysics with the Square Kilometre Array (AASKA14)*, p. 37
- Johnson J. L., Greif T. H., Bromm V., 2008, *MNRAS*, **388**, 26
- Katz H., Sijacki D., Haehnelt M. G., 2015, *MNRAS*, **451**, 2352
- Kauffmann G., Haehnelt M., 2000, *MNRAS*, **311**, 576
- Kawamura S., et al., 2006, *Classical and Quantum Gravity*, **23**, S125
- Kidder L. E., Will C. M., Wiseman A. G., 1993, *Phys. Rev. D*, **47**, 3281
- King A., 2003, *ApJ*, **596**, L27
- Kormendy J., Ho L. C., 2013, *ARA&A*, **51**, 511
- Koushiappas S. M., Zentner A. R., 2006, *ApJ*, **639**, 7
- Koushiappas S. M., Bullock J. S., Dekel A., 2004, *MNRAS*, **354**, 292
- Lagos C. d. P., et al., 2015, *MNRAS*, **452**, 3815
- Loeb A., Rasio F. A., 1994, *ApJ*, **432**, 52
- Lupi A., Colpi M., Devecchi B., Galanti G., Volonteri M., 2014, *MNRAS*, **442**, 3616
- Madau P., Rees M. J., 2001, *ApJ*, **551**, L27
- Magorrian J., et al., 1998, *AJ*, **115**, 2285
- McAlpine S., et al., 2015, preprint, ([arXiv:1510.01320](#))
- Misner C. W., Thorne K. S., Wheeler J. A., 1973, *Gravitation*
- Moore C. J., Cole R. H., Berry C. P. L., 2015, *Classical and Quantum Gravity*, **32**, 015014
- Ohme F., 2012, *Classical and Quantum Gravity*, **29**, 124002
- Omukai K., 2001, *ApJ*, **546**, 635
- Planck Collaboration et al., 2014, *A&A*, **571**, A16
- Price D. J., 2008, *Journal of Computational Physics*, **227**, 10040
- Quinlan G. D., 1996, *New Astron.*, **1**, 35
- Rahmati A., Schaye J., Crain R. A., Oppenheimer B. D., Schaller M., Theuns T., 2015a, preprint, ([arXiv:1511.01094](#))
- Rahmati A., Schaye J., Bower R. G., Crain R. A., Furlong M., Schaller M., Theuns T., 2015b, *MNRAS*, **452**, 2034
- Regan J., Johansson P., Wise J., 2015, preprint, ([arXiv:1511.00696](#))
- Reines A. E., Greene J. E., Geha M., 2013, *ApJ*, **775**, 116
- Rosas-Guevara Y. M., et al., 2015, *MNRAS*, **454**, 1038
- Schaller M., et al., 2015a, *MNRAS*, **451**, 1247
- Schaller M., Dalla Vecchia C., Schaye J., Bower R. G., Theuns T., Crain R. A., Furlong M., McCarthy I. G., 2015b, *MNRAS*, **454**, 2277
- Schaye J., 2004, *ApJ*, **609**, 667
- Schaye J., Dalla Vecchia C., 2008, *MNRAS*, **383**, 1210
- Schaye J., et al., 2015, *MNRAS*, **446**, 521
- Schutz B. F., Ricci F., 2010, preprint, ([arXiv:1005.4735](#))
- Segers M. C., Crain R. A., Schaye J., Bower R. G., Furlong M., Schaller M., Theuns T., 2015, preprint, ([arXiv:1507.08281](#))
- Sesana A., 2012, *Advances in Astronomy*, **2012**, 12
- Sesana A., Volonteri M., Haardt F., 2007, *MNRAS*, **377**, 1711
- Sesana A., Vecchio A., Colacino C. N., 2008, *MNRAS*, **390**, 192
- Sesana A., Gair J., Berti E., Volonteri M., 2011, *Phys. Rev. D*, **83**, 044036
- Seth A., Agüeros M., Lee D., Basu-Zych A., 2008, *ApJ*, **678**, 116
- Seth A. C., et al., 2014, *Nature*, **513**, 398
- Shapiro S. L., Teukolsky S. A., 1983, *Black holes, white dwarfs, and neutron stars: The physics of compact objects*
- Springel V., 2005, *MNRAS*, **364**, 1105
- Springel V., Di Matteo T., Hernquist L., 2005, *MNRAS*, **361**, 776
- Sugimura K., Omukai K., Inoue A. K., 2014, *MNRAS*, **445**, 544
- Tinto M., 1988, *American Journal of Physics*, **56**, 1066
- Trayford J. W., et al., 2015, *MNRAS*, **452**, 2879
- Volonteri M., 2010, *A&ARv*, **18**, 279
- Volonteri M., Bellovary J., 2011, in von Berlepsch R., ed., *Reviews in Modern Astronomy Vol. 23, Reviews in Modern Astronomy*. p. 189, doi:10.1002/9783527644384.ch11
- Volonteri M., Bellovary J., 2012, *Reports on Progress in Physics*, **75**, 124901
- Volonteri M., Haardt F., Madau P., 2003, *ApJ*, **582**, 559
- Volonteri M., Habouzit M., Pacucci F., Tremmel M., 2015, preprint, ([arXiv:1511.02588](#))
- Wendland H., 1995, *Advances in Computational Mathematics*, **4**, 389
- Wiersma R. P. C., Schaye J., Smith B. D., 2009a, *MNRAS*, **393**, 99
- Wiersma R. P. C., Schaye J., Theuns T., Dalla Vecchia C., Tornatore L., 2009b, *MNRAS*, **399**, 574
- Wyithe J. S. B., Loeb A., 2003, *ApJ*, **590**, 691

## APPENDIX A: PARAMETER VARIATIONS

In this section we test our predictions against variations of the different parameters and assumptions used in our calculations. The parameters that we vary are:

- Low-frequency cut-off of the sensitivity curve of the detector ( $f_{\text{cut}}$ )
  - Bandwidth requirement ( $10^{-4}$  Hz to 1 Hz)
  - Bandwidth target ( $3 \times 10^{-5}$  Hz to 1 Hz)
  - Optimistic bandwidth ( $10^{-5}$  Hz to 1 Hz)
- Efficiency of the energy radiated during the merging phase ( $\epsilon_{\text{merger}}$ )
  - Low (3%) for merging BHs with no spin
  - High (10%) for rapidly spinning coalescing BHs
- Simulated volume
  - Ref-L100N1504 with volume  $(100 \text{ cMpc})^3$
  - Ref-L050N0752 with volume  $(50 \text{ cMpc})^3$
  - Ref-L025N0376 with volume  $(25 \text{ cMpc})^3$
- Resolution
  - Reference model ‘Ref’ (with baryonic particle mass  $M_{\text{gas}} = 1.81 \times 10^6 M_{\odot}$ , dark matter particle mass  $M_{\text{gas}} = 9.70 \times 10^6 M_{\odot}$ , co-moving gravitational softening  $\epsilon_{\text{com}} = 2.66 \text{ ckpc}$ , and maximum proper gravitational softening  $\epsilon_{\text{prop}} = 0.70 \text{ ckpc}$ )

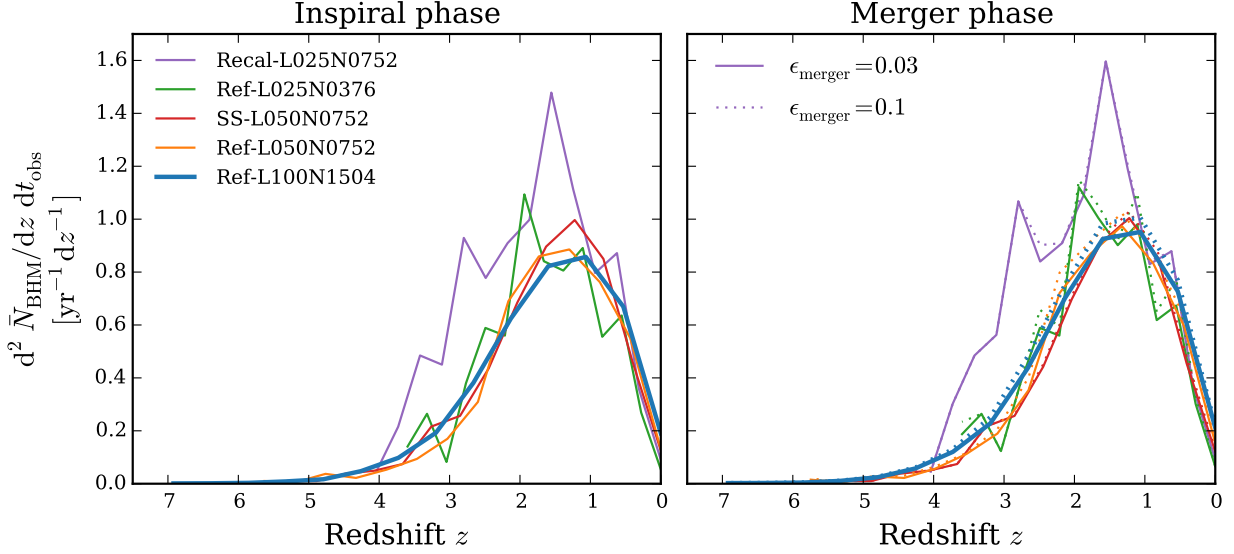


**Figure A1.** Number of SMBH coalescences resolved by eLISA ( $f_{\text{cut}} = 3 \times 10^{-5}$  Hz) per observed year, per unit redshift. *LEFT PANEL:* inspiral phase. *RIGHT PANEL:* merger phase. Solid lines were calculated using a gravitational radiation efficiency of  $\epsilon_{\text{merger}} = 0.03$ . For the dotted lines  $\epsilon_{\text{merger}} = 0.1$ . The distribution peaks between redshift  $z \sim 2$  and  $z \sim 1$  for both the inspiral and the merger phases.

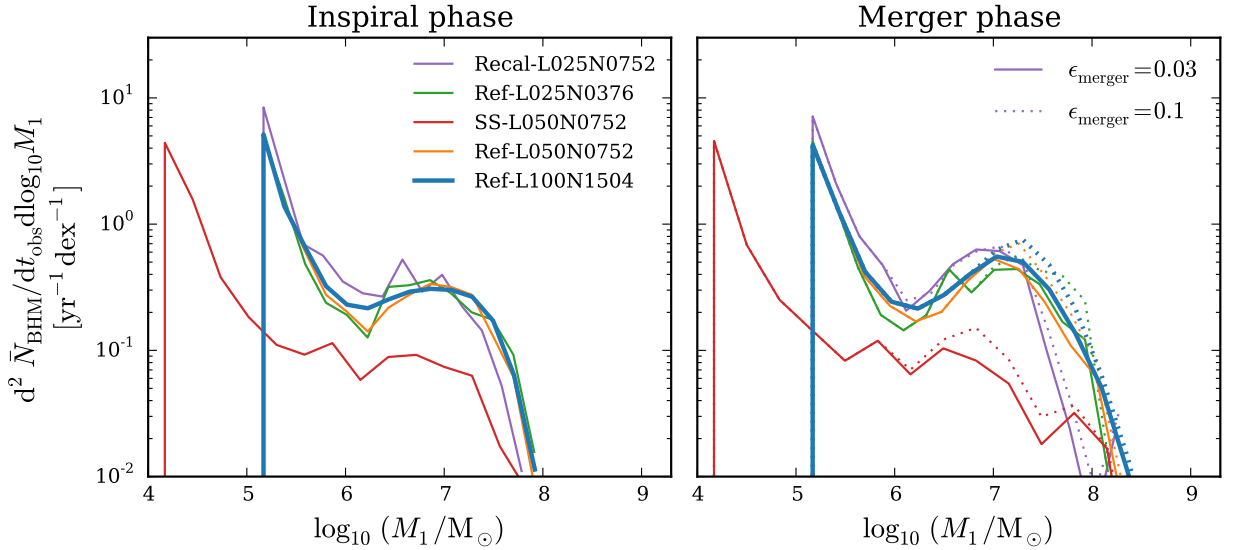


**Figure A2.** Distribution of mass of the more massive member of the binary,  $M_1$ , of the SMBH coalescences resolved by eLISA ( $f_{\text{cut}} = 3 \times 10^{-5}$  Hz). *LEFT PANEL:* inspiral phase. *RIGHT PANEL:* merger phase. Solid lines were calculated using a gravitational radiation efficiency  $\epsilon_{\text{merger}} = 0.03$ . For dotted lines  $\epsilon_{\text{merger}} = 0.1$ . The distribution peaks at  $M_1 \sim m_{\text{seed}}$  for both the inspiral and the merger phases.

– High-resolution recalibrated model ‘*Recal*’ (with baryonic particle mass  $M_{\text{gas}} = 2.26 \times 10^5 M_{\odot}$ , dark matter particle mass  $M_{\text{gas}} = 1.21 \times 10^6 M_{\odot}$ , co-moving gravitational softening  $\epsilon_{\text{com}} = 1.33$  ckpc, and maximum proper gravitational softening  $\epsilon_{\text{prop}} = 0.35$  ckpc).

We show in Fig. A1 the redshift distribution of the eLISA SMBH coalescence detections for both the inspiral and merger phases ( $f_{\text{cut}} = 3 \times 10^{-5}$  Hz). The event rates for two gravitational radiation efficiencies,  $\epsilon_{\text{merger}}$ , are shown in the right panel. We obtain consistent results for the different

EAGLE simulation models used in this study, where for both the inspiral and merger phases the redshift distribution of the event rate peaks between redshift  $z \approx 2$  and  $z \approx 1$ .

In Fig. A2 we show the mass function of the more massive member of the binary,  $M_1$ , for the SMBH coalescences resolved by eLISA ( $f_{\text{cut}} = 3 \times 10^{-5}$  Hz). For the merger phase the two gravitational radiation efficiencies,  $\epsilon_{\text{merger}}$ , used in the analysis are shown in the right panel. For both the inspiral and merger phases the mass function has a very pronounced peak at  $M_1 \sim m_{\text{seed}}$ . Given the logarithmic scale of the plot,

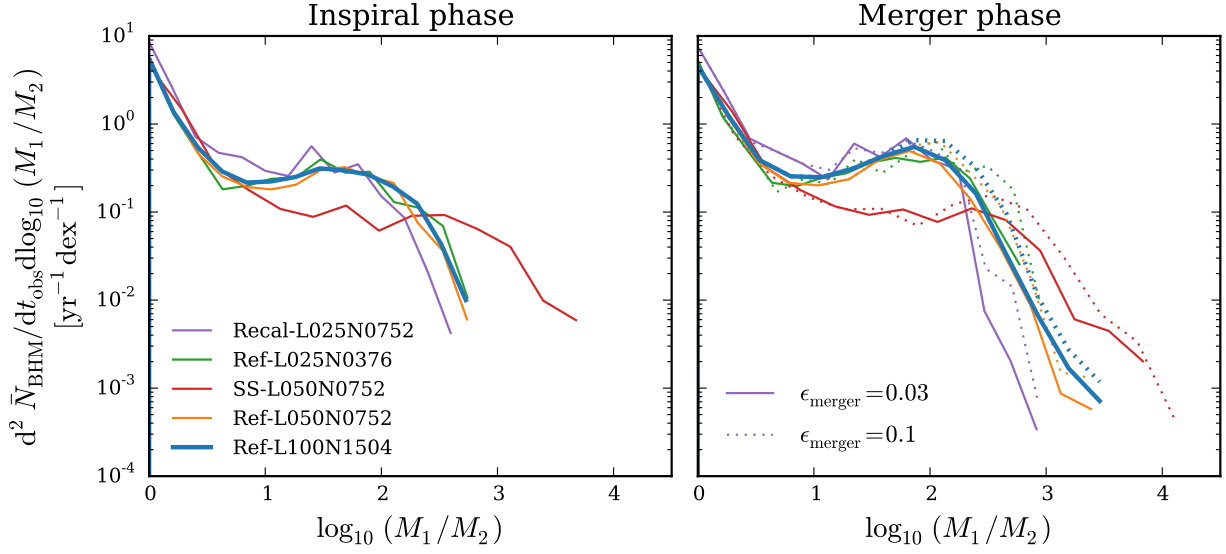


**Figure A3.** Distribution of the mass ratio,  $M_1/M_2$ , of the SMBH coalescences resolved by eLISA ( $f_{\text{cut}} = 3 \times 10^{-5}$  Hz). *LEFT PANEL:* inspiral phase. *RIGHT PANEL:* merger phase. Solid lines were calculated using a gravitational radiation efficiency  $\epsilon_{\text{merger}} = 0.03$ . For dotted lines  $\epsilon_{\text{merger}} = 0.1$ . The distribution peaks at equal mass SMBH binaries for both the inspiral and the merger phase.

the galaxy formation model implemented in EAGLE predicts that GW signals will be dominated by the coalescence of BH seeds (also shown in Fig. A3, in which the mass distribution of the mass ratio  $M_1/M_2$  of the predicted event rate is dominated by equal mass SMBH coalescences).

Our event rate predictions are robust to variations of simulated volume, resolution, and parameters used to calculate the GW detections of the eLISA detector such as,  $f_{\text{cut}}$  and  $\epsilon_{\text{merger}}$ . We summarise in Table T1 the predicted event rates for both the inspiral and merger phases for all the different parameter variations, simulated volumes and resolutions. Overall, the predicted event rates of GW signals resolved by the eLISA detector are  $\sim 2$  events per year for all the reference models, whereas the high-resolution recalibrated model Recal-L025N0752 yields  $\sim 3$  events per year. This does not represent a significant change in the predicted event rate.

This paper has been typeset from a  $\text{\LaTeX}$  file prepared by the author.



$f_{\text{cut}}$ [Hz]	$\epsilon_{\text{mer}}$	Simulation	Inspiral Phase event rate [yr <sup>-1</sup> ]	Merger Phase event rate [yr <sup>-1</sup> ]
$1 \times 10^{-5}$	0.03	Ref-L100N1504	1.94	2.16
		SS-L050N0752	1.96	1.96
		Ref-L050N0752	1.87	2.03
		Ref-L025N0376	1.93	2.06
		Recal-L025N0752	2.83	3.05
	0.10	Ref-L100N1504	1.94	2.31
		SS-L050N0752	1.96	2.01
		Ref-L050N0752	1.87	2.17
		Ref-L025N0376	1.93	2.20
		Recal-L025N0752	2.83	3.08
$3 \times 10^{-5}$	0.03	Ref-L100N1504	1.91	2.15
		SS-L050N0752	1.95	1.96
		Ref-L050N0752	1.85	2.03
		Ref-L025N0376	1.90	2.06
		Recal-L025N0752	2.82	3.05
	0.10	Ref-L100N1504	1.91	2.30
		SS-L050N0752	1.95	2.00
		Ref-L050N0752	1.85	2.17
		Ref-L025N0376	1.90	2.20
		Recal-L025N0752	2.82	3.08
$1 \times 10^{-4}$	0.03	Ref-L100N1504	1.80	2.12
		SS-L050N0752	1.93	1.95
		Ref-L050N0752	1.76	2.00
		Ref-L025N0376	1.82	2.05
		Recal-L025N0752	2.76	3.04
	0.10	Ref-L100N1504	1.80	2.26
		SS-L050N0752	1.93	1.99
		Ref-L050N0752	1.76	2.14
		Ref-L025N0376	1.82	2.19
		Recal-L025N0752	2.76	3.08

**Table T1.** Estimated event rates for different parameter and box size variations.